Influence of gas atmosphere (Ar or He) on the laser powder bed fusion of a Ni-based alloy

S. Traore[a,b,*], M. Schneider[a], I. Koutiri[a], F. Coste[a], R. Fabbro[a], C. Charpentier[b], P. Lefebvre[b], P. Peyre[a]

[a] Laboratoire PIMM, Arts Et Métiers Institute of Technology, CNRS, Cnam, HESAM University, 75013 Paris, France
[b] Air Liquide Paris Innovation Campus, 1 Chemin de la Porte des Loges, 78350, Les Loges-en-Josas, France

A B S T R A C T

The gaseous atmosphere plays a major role in the quality of the manufactured parts in Laser Powder Bed Fusion (L-PBF) by protecting the metal from high temperature oxidation. If argon and nitrogen are the most commonly used gases, helium has almost never been considered as a possible candidate as a chemically inert shielding gas. To provide a better understanding of the influence of the gas atmosphere on the process stability, a comparative study of L-PBF manufacturing under argon and helium atmospheres has been carried out, considering a nickel-based alloy Inconel® 625 and a single bead configuration. To this end, in-situ process measurements were carried out on a dedicated experimental setup. The melt pool behaviour, the expansion of the vapour plume and the amount of spatters were evaluated with high-speed imaging for the two gases considered, together with the final L-PBF bead dimensions. Results were also compared to single fusion beads carried out in an industrial L-PBF machine for a comparable range of volume energy densities. The influence of the shielding atmosphere on L-PBF single beads was as follows: (1) dimensions of beads were shown to be constant whatever the gas; (2) fewer and smaller spatters were produced under helium atmosphere, especially for high volume energy densities. Physical mechanisms were then discussed to understand those specific effects.

1. Introduction

The Laser Powder Bed Fusion (L-PBF) process is an additive manufacturing technique based on the high-speed scanning (at around 1 m/s) of a powder bed with a laser beam. For each layer, the laser follows a path defined by the slicing of the desired object's 3D model. Commonly, a small laser beam (diameter d < 100 μm) irradiates powder layers of a few tens of microns in thickness and generates a small melt pool involving high thermal gradients and cooling rates (10^{5-6} K/s). Due to the high-speed hydrodynamic flow inside the melt pool, several instabilities like liquid spatters or melt pool fluctuations also occur, which can potentially be detrimental to the final properties (surface finish, porosity rate) of built parts.

The optimisation of the large number of L-PBF parameters is the key to obtain fully dense matter and prevent instabilities. However, the gaseous environment is usually considered as negligible versus the well-known effect of first order parameters such as laser power, scan speed, hatch distance or layer thickness. For the vast majority of conditions reported in the literature, argon and nitrogen are the most often used gases in L-PBF working chambers, with O_2 rates varying between 20 ppm and 2000 ppm.

Protective gases have distinct physical characteristics that can alter the L-PBF process, either by interacting with the incident laser irradiation through a modification of vapour plume properties or by modifying the melt pool properties due to specific boundary conditions (wide range of thermal conductivities) or surface tension effects. Many authors have considered the effect of gaseous atmosphere on the quality (shape and microstructures) of weld beads in high power CO_2 laser welding (λ = 10.6 μm). One of the most significant effects is the difference in welding penetration (Glowacki, 1995) attributed it to the defocusing of the incident laser and to the absorption of incoming laser energy by a high temperature plasma. This specific behaviour of CO_2 laser induced plumes is attributed to the main absorption mechanism in the plasma, known as Inverse Bremsstrahlung (IB) which absorption coefficient is proportional to the square of the laser wavelength (Matsunawa and Kim, 2006). Increasing the proportion of helium in the gas mixture minimizes refraction phenomena and resulting defocusing effects thus improving energy coupling. Moreover, for a temperature in the plume of around 20 000 K, the absorption coefficient in pure argon is 7 times greater than in pure helium. The resulting effect is up to 20

* Corresponding author at: Laboratoire PIMM, Arts et Métiers Institute of Technology, CNRS, Cnam, HESAM University, 75013 Paris, France.
E-mail address: socona.traore@ensam.eu (S. Traore).

Table 1
Properties of Ar, He and N_2 gases (at 25 °C and 1 atm) *(Air Liquide, 2020)*.

Properties	Argon	Helium	Nitrogen
Density [kg. m^{-3}]	1.63	0.16	1.15
Thermal conductivity [mW. m^{-1}. K^{-1}]	17.75	155.3	25.84
Heat capacity at constant pressure [J. kg^{-1}. K^{-1}]	522	5193	1041
Thermal diffusivity [$mm^2.s^{-1}$]	21	183	22
Ionization energy [eV]	15.76	24.56	15.58

times deeper penetrations in 100 % helium than in 100 % argon (Katayama, 2010) for high intensity CO_2 laser welding. During metallic welding, two kinds of plasmas are prone to occur: a metallic plasma and a gas plasma (Hoffman and Szymanski, 2004). Preventing the formation of a gas plasma is favoured by high ionization energy gas. Due to the higher ionization energy of helium (around 25 eV vs. 16 eV for Argon (Table 1)), the absence of gas plasma under helium atmosphere might be the reason for deeper welding beads.

Mainly Yb:YAG lasers are used in L-PBF, with 10 times lower wavelength ($\lambda \sim 1.07$ µm) than with CO_2 laser resulting in IB absorption coefficient of a hundred times lower. For this reason, highly absorptive plasma plumes are unlikely during L-PBF process for which the absorption is too weak to modify the energy coupling. The plume is rather composed of a weakly ionized vapour than of a real plasma (with a much higher free electron density), (Shcheglov et al., 2013).

Focusing on the keyhole-welding mode with a fiber laser ($\lambda = 1.07$ µm), (Ahn et al., 2017) evaluated laser welds obtained under argon or helium shielding. At very high energy density, the higher ionization potential of helium limits vapour plume effects, and was shown to result in wider and deeper melt pools. However, this work cannot be directly extrapolated to the L-PBF because it was conducted in a classical welding mode (low welding speed < 5 m/min), and with a local gas shielding, i.e. using a nozzle. (Greses et al., 2004) have proposed an experimental and analytical procedure to investigate the laser-induced vapour plume properties, and its possible interactions with YAG incident laser light during laser welding. One of his main conclusions is that Rayleigh absorption on nanoparticles is the dominant mechanism to consider in laser/vapour interaction. (Kuo and Lin, 2007) studied the influence of different shielding gas (argon, helium and nitrogen) during YAG pulsed laser welding of Inconel 690. They obtained similar weld beads dimensions and spatter generation whatever the protective gas and its flow rate but they reported that welding under helium generated a reduced vapour plume due to its higher thermal conductivity, and a faster expansion due to its lower density. The higher amount of porosities was obtained with argon whereas nitrogen gave the lower porosity rate because of probable surfactant effect of the gas, lowering melt pool surface tension and favouring degassing.

Until now, few authors have considered the gaseous influence on the L-PBF process stability or the density of manufactured parts. (Dai and Gu, 2015) investigated numerically and experimentally the comparative effect of argon, helium and nitrogen on the fusion mode stability of an aluminium matrix composite. In their numerical work, they claimed that argon and nitrogen have a stabilizing effect on the process, whereas helium promotes fluctuations of penetration depth. They correlated those fluctuations to the surface quality: the more stable the keyhole, the smoother the surface finish. The resulting effect was a much higher densification of manufactured parts in Ar (99 %) than in He and N_2 (85 % and 91 %) for similar L-PBF conditions. Significantly different results were obtained by (Wang et al., 2014) on a Al-12 Si cast alloy using Ar, He and N_2 shielding. For the three gases considered, similar – but rather low - densification rates (~ 97 %) were obtained, and a lower ductility was evidenced during tensile tests on He-shielded samples. This reduced ductility was attributed to the presence of a cluster of porosities in the solidified material due to the inclusion of micro helium bubbles in the melt pool. More recently, (Charpentier et al., 2018) have shown that during powder bed fusion of Ti-6Al-4 V, a higher number of nanoaggregates is generated inside chambers filled with helium rather than with argon. They also observed a faster contamination of the chamber with vapour fumes under helium.

(Bidare et al., 2018) investigated the influence of gaseous atmosphere for pressures comprised between 1 and 5 bars. The use of helium was found to be beneficial at high pressure, with a more stable process, a constant amount of spatters and smoother bead surfaces with increasing power. Deeper beads were also observed with helium because of faster plume expansion (lower density and kinematic viscosity) resulting in a reduced attenuation of the incident laser. By extrapolating, an increase in process speed might be foreseen under helium gas. Last but not least, the influence of gas flow direction versus scanning direction is also an important parameter to be considered in L-PBF. For instance (Anwar and Pham, 2017) indicated that scanning against gas flow (opposite direction) with high gas velocity resulted in better UTS (Ultimate Tensile Strength). (Andreau et al., 2019) also obtained deeper penetration on 316 L steel when scanning perpendicularly to the gas flow, due to a lower attenuation of laser with vapour fumes.

Finally, considering the limited number of available works, it can be concluded that there is a global lack of data and understanding on the effect of building atmosphere in L-PBF. This is particularly obvious at the laser-powder bed-melt pool interaction scale. Three main aspects are supposed to be influenced by the L-PBF gas atmosphere:

- The laser – melt pool energy coupling, and the vapour plume (size, density, shape) properties
- The melt pool dynamics: oscillations, surfactant effects
- The aerodynamic phenomena surrounding melt pools: and its resulting effects like particles dragging or gas recirculation as shown by (Matthews et al., 2016) and (Guo et al., 2018)

In the current investigation, a series of single L-PBF beads were carried out on a manually pre-deposited powder bed of Inconel 625 using a dedicated instrumented cell allowing a precise control of the shielding atmosphere and high-speed imaging of the process. The choice of Inconel 625 was driven by the current developments of Air Liquide in the field of hydrogen production with intensified reactors produced by L-PBF (FAIR project) for which a high temperature resistance (800–900 °C) was mandatory. Moreover, because Inconel 625 is a relatively well-known L-PBF material, it was considered as a good candidate to investigate the influence of a new parameter like gaseous atmosphere. Single bead-on-plate experiments (without powder) were also realised with the same setup. Additionally, L-PBF beads were also produced using an industrial machine under argon and helium atmospheres. As developed in the work of (Bosio et al., 2019), the analysis of properties in single bead configuration is the very first step of parametric optimisation, the single beads characteristics are strongly affecting the quality of the subsequent 3D parts.

The objectives of the current work were: (1) to provide a deeper understanding of the influence of gas atmosphere (He/Ar) in L-PBF, (2) to compare beads on-plate and L-PBF configurations, (3) to validate the use of a dedicated experimental L-PBF cell to analyse the influence of gas shielding, and compare it to industrial conditions.

For this purpose, bead dimensions, melt pool properties, denudation phenomena, vapour plumes and spatters ejections have been considered.

2. Experimental procedure

2.1. L-PBF conditions

The main differences between the two L-PBF configurations used in this study are as follows (Fig. 1): on the instrumented set-up, the powder bed substrate, positioned into a small gas cell, moves below a static laser beam contrary to the scan head irradiation used on the SLM 125 machine, where only laser spot moves and the powder bed is static.

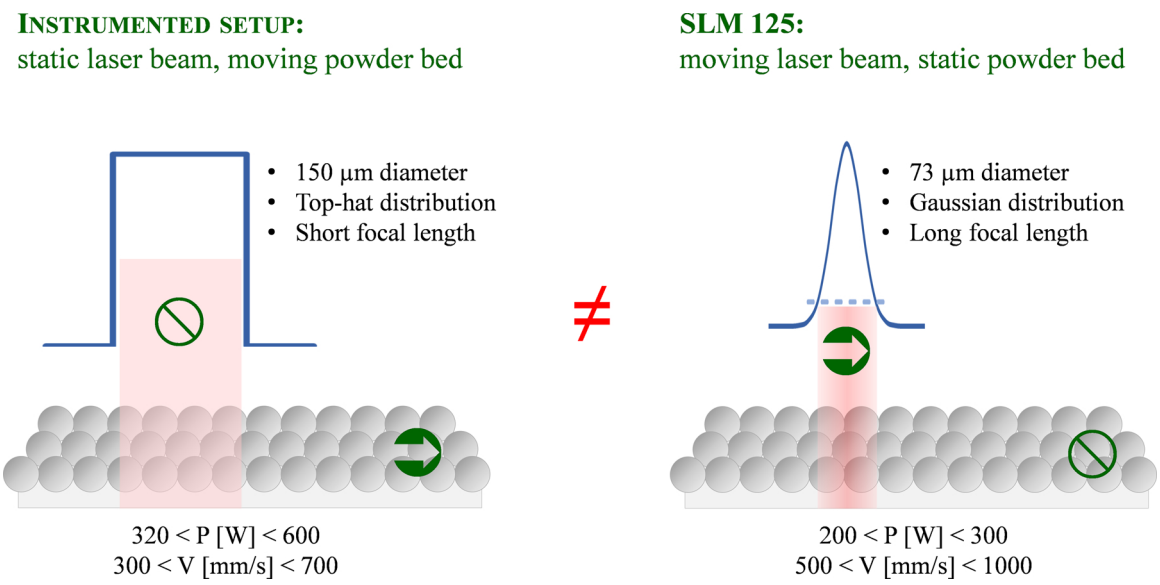

Fig. 1. Schematic description of the main L-PBF conditions for each setup.

The laser spots (distribution and size) are different: a 150 µm diameter top hat for the instrumented set-up and a 73 µm diameter Gaussian spot for the SLM 125 industrial machine.

2.1.1. L-PBF tests in the open L-PBF cell

A dedicated L-PBF cell was designed for this experimental study (Fig. 2.). A 10 kW Yb:YAG (λ = 1.03 µm) laser disc source (Trumpf TruDisk 10,002) was focused into a 150 µm diameter "top hat" laser beam at the focus point by the use of collimating (f 200) and focusing (f 150) lenses. The L-PBF chamber was manufactured with the Visijet M3 resin from 3D Systems. Its small volume (less than 2 L) allowed modifying easily and controlling precisely the working atmosphere. The gas is injected through two inlets and a non-return valve prevents the flow of the outside ambient air towards the inside of the chamber. Argon and helium inert gases were selected because of their very different physical properties (Table 1), argon being ten times denser than helium and having a nine times lower thermal conductivity. The measurement of O2 rate was ensured using an O2 analyser (ZRA II MP of ARELCO®). With incoming gas flow rates of 10 L/min, O2 rates of less than 50 ppm were reached in less than one minute pumping time. Five windows on the chamber allow laser access and viewing of the interaction. A pure silica glass window at the top of the cell allows a full transmission of laser light, and four other windows (two laterals and two inclined) are used to carry out high-speed imaging and illumination of the L-PBF scene.

The main difference with usual L-PBF process with scan heads is that here the powder substrate moves below a static laser beam, with a motorized linear table reaching up to 1 m/s speed. This "static beam"

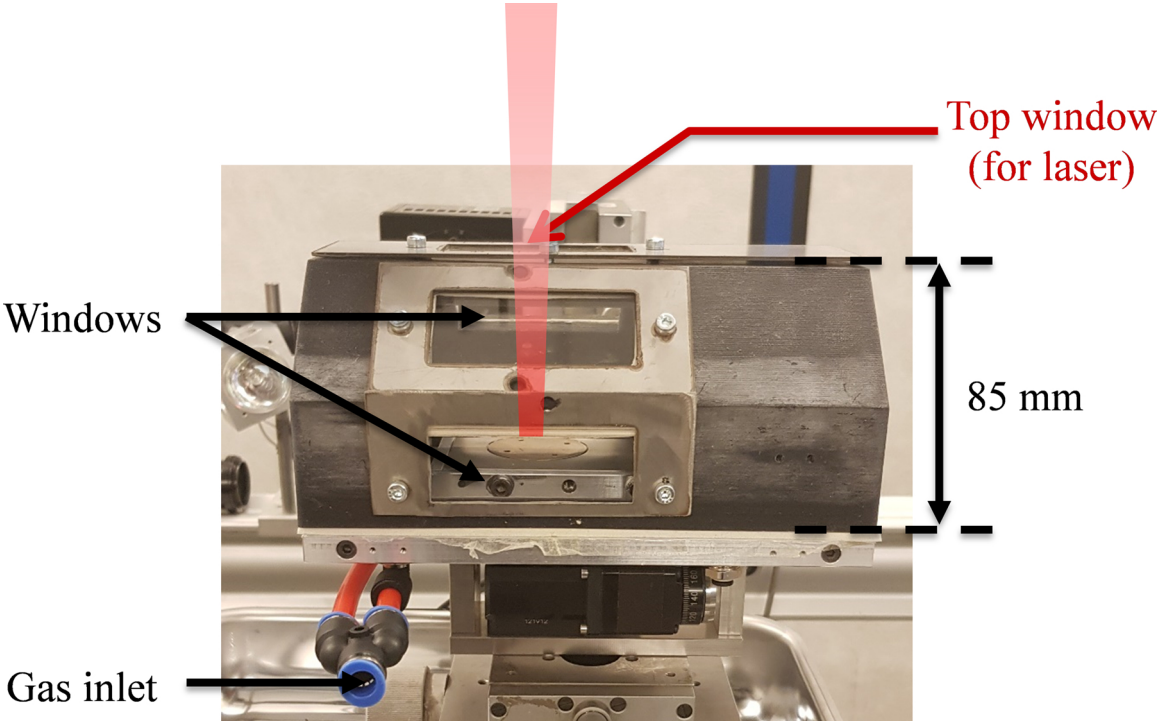

Fig. 2. Side view of the L-PBF working chamber.

Table 2
Parameters of the experimental study in the open setup (static beam, moving substrate).

VED [J/mm^3]		Laser power [W]			
		320	400	500	600
Speed [mm/s]	300	60	75	94	113
	500	36	45	57	68
	700	26	32	40	49
I [MW/cm2]		1.8	2.3	2.8	3.4

setup facilitates the high-resolution monitoring of the fusion zone and its surroundings. As the laser is kept static, the system allows continuous monitoring of the laser-melt pool interaction, in contrast to recent instrumented set-ups used for instance by (Bidare et al., 2017). For one single bead a volume energy density (VED) was defined to represent the instantaneous energy provided by the laser for one volume unit of metal material. It was obtained by dividing the laser intensity I (Eqn (1)) by the scanning speed V_0 (Eqn (2)). In the current work, the laser power ranged from 320 to 600 W and the scan velocity from 0.3 to 0.7 m/s. Therefore, for a d = 150 µm beam diameter, the VED range was between 26 and 113 J/mm^3, and the intensity from 1.8 to 3.4 MW/cm^2. (Table 2). The VED range correspond to classical L-PBF conditions where the Inconel 625 gives regular and continuous single beads without instabilities like humping or balling.

$$I = \frac{4\,P_0}{\pi\,d^2} \tag{1}$$

$$VED = \frac{I}{V_0} = \frac{4\,P_0}{\pi\,V_0\,d^2} \tag{2}$$

With: I [MW/cm^2] = Laser intensity; VED [J/mm^3] = Volume Energy Density; P_0 [W] = laser power; V_0 [mm/s] = scan speed and d [mm] = beam diameter.

2.1.2. L-PBF tests in the SLM 125 HL machine

A SLM 125 HL industrial L-PBF machine from SLM Solutions Gmbh was also used, with a Gaussian laser beam of d = 73 µm diameter, two times smaller than the one used on the previous setup. Moreover, the focal length is longer (420 mm vs. 150 mm) and the volume of the manufacturing chamber is larger than the open setup volume (around 50 L).

For each protective gas, three samples (namely 1, 2, and 3) were placed in the chamber (Fig. 3) with the gas always entering by the same side. On each sample, single L-PBF beads were produced using two laser powers (200 and 300 W) and three scanning speeds (500, 750 and 1000 mm/s) (Table 3), corresponding to VED values between 48 and 143 J/mm^3. All beads were built perpendicularly to the gas flow.

2.2. Materials and powder bed samples

Inconel® 625 is a nickel-chromium based alloy, widely used for its high corrosion and oxidation resistance and good mechanical resistance at high temperature. Although the material is already well known (in a given process window, Inconel 625 shows stable melt pools and very good densification under argon shielding), it can still be further improved with parameters optimisation, for instance in terms of build rate. It was also ideal to check if changing the gaseous atmosphere is upgrading or downgrading these properties and suitable to detect at which steps of the interaction the gas is affecting the process. Here, it was used for both the substrates and the powder. The powder supplier provided the chemical composition (Table 4) and it was determined using ICP Spectroscopy method (Inductively Coupled Plasma). Powder distribution and morphology was analysed using CILAS Particle Size 920 L granulometer and HITACHI 4800 II electron beam microscope. A mean diameter of 25 µm, a d10 of 11 µm, a d50 of 22 µm and a d90 of 42 µm were measured (Fig. 4.b). Moreover, SEM imaging (Fig. 4.a) evidenced mostly spherical powder grains of various sizes. L-PBF samples were composed of a 3 mm thick Inconel 625 plates covered with a manually spread- powder bed using a razor blade, providing an estimated powder bed compactness of 48 %. The layer thickness was controlled by optical profilometry and was near 80 µm. Similar samples were used on the two experimental setups. As a comparison, bead-on-plate fusion lines were carried on bare Inconel 625 plate (without powder).

2.3. Measurements and analyses

To investigate the influence of gas shielding, the following analyses were conducted:

- High-speed imaging of the melt pools, plume expansion and spatters ejection
- Collection of ejected spatters and condensates
- Post-mortem analyses of L-PBF beads (optical microscopy and optical profilometry)

2.3.1. High-speed imaging

A *UX100 Mini Photron* Fastcam, high-speed camera is used for the high-speed imaging of melt pools and spatters. Such a camera allows frequency rates of 4 kiloframes per second (kfps) with a full resolution of 1 280 × 1 024 pixels and higher frequencies for reduced windows. Depending on the type of experimental test (Fig. 5), two configurations were used on the instrumented set-up:

- The side analysis at 10 kfps of the vapour plume and spatters ejections on a 5.7 mm x 10.5 mm window (12 µm/pixel) with the camera positioned perpendicularly to the laser beam axis and without additional lightning (Fig. 5, right)
- The high-resolution analysis of the melt pool and surrounding powder bed dynamics on a 3.4 mm x 0.8 mm window (3 µm/pixel), with a 60° inclination of the camera. In that case, the high-speed (16 kfps) imaging was synchronized with an 810 nm laser diode illumination (Cavilux® system) (Fig. 5, left).

In the industrial L-PBF machine using a scan head, the previously described instrumentation is impossible because the laser and the interaction zone are always in motion. Moreover, the control window used for observing fusion zone is rather far from the powder bed. For this reason, only a low-resolution imaging was used, with 68 µm/pixel and 2000 fps (Fig. 6). Such movies only allow checking whether or not the surrounding atmosphere affects the amount of spatters generated during the fusion.

2.3.2. Post-mortem analyses

L-PBF beads and surrounding powder bed were analysed post-mortem using optical microscopy and optical profilometry to provide information about beads geometry and denuded areas. An example of optical profile is shown in Fig. 7, where the L-PBF bead height is approximately equal to the powder bed thickness (≈ 80 µm) but with a large denudation on both lateral sides of the bead. Additionally, metallurgical observations of fusion beads were carried out on cross sections after a dedicated metallographic preparation (with a diamond polishing up to 0.25 µm, and a chemical etching using 92 % HCl, 5 % H_2SO_4 and 3 % NHO_2). This allowed measuring the beads' dimensions (depth, height, width and surface) from the macrographs (Fig. 9. a.). For each (P, V) couple, three beads were made and each bead was cut in three zones (Fig. 8). Hence, standard deviations were estimated from at least nine experimental values.

Lastly, to analyse the particles constituting the vapour plume and the spatters ejected backwards during L-PBF, a glass slide was positioned 3 mm above the sample in order to collect the condensed fumes

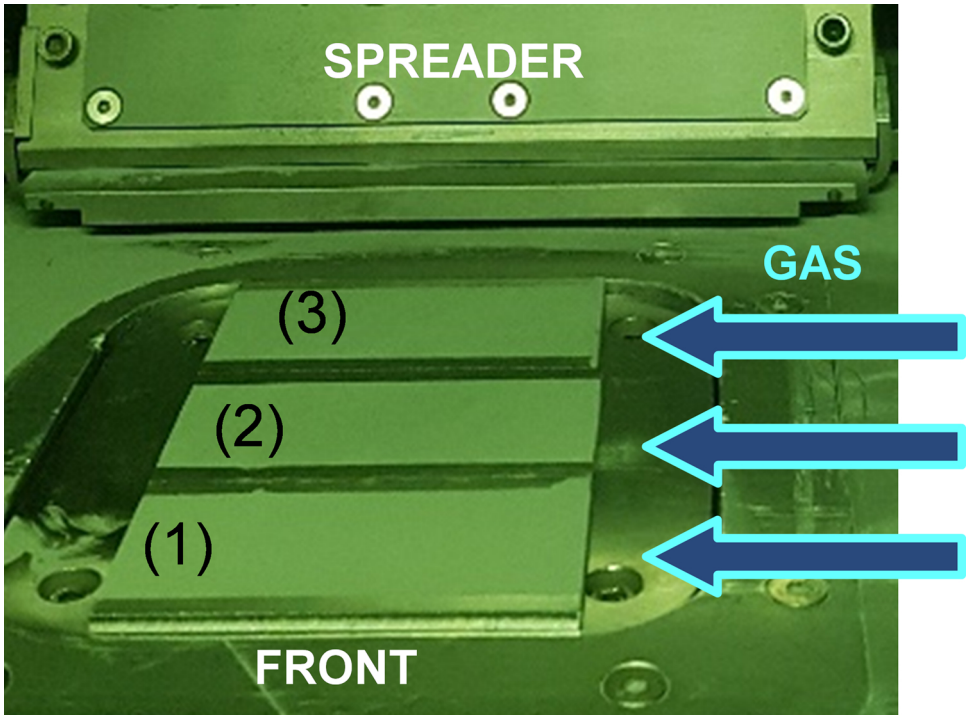

Fig. 3. Positioning of samples in the SLM 125 working chamber.

Table 3
Parameters of the experimental study in the SLM 125 HL (moving beam, static substrate).

VED [J/mm^3]		Laser power [W]	
		200	300
Speed [mm/s]	500	96	143
	750	64	96
	1000	48	72
I [MW/cm^2]		4.8	7.2

Table 4
Composition of the Inconel® 625 alloy.

Elements	Ni	Cr	Fe	Mo	Nb	Co	C, Mn, Si, P, S, Al, Ti
% mass	63.80	22.16	0.30	9.20	3.66	0.30	< 0.20

and emitted spatters during single bead fusion. The glass slides were also weighed before and after fusion before performing SEM (Scanning Electron Microscopy) and EDS (Energy-dispersive X-ray Spectroscopy) analysis of the condensed particles in the collected vapour and spatters.

3. Experimental results on instrumented set-up

3.1. Analysis of molten surfaces for on-plate and powder bed fusions

In a first step, single beads were observed from the top, to identify possible fusion instabilities (like balling and humping..;). However, most of beads were regular in shape and width. No clear difference in terms of track's stability was shown with the use of Ar or He. For this reason, we did not consider classical process stability diagram (P versus V). Dimensions and areas of beads were estimated from the optical microscopy cross-sections. At first glance, the global morphologies (Fig. 9.a) seem identical in Ar or He whatever the tested parameters, with an increase in penetration depth, manufactured height and width depending on laser power.

For each fusion mode (bead-on-plate or L-PBF), molten surfaces (S_m) are very similar for argon and helium (Fig. 9.b). It indicates that the global laser-matter interaction conditions, and the average absorbed energy, are globally unchanged between argon and helium. It also implies that the higher thermal diffusivity of helium did not have a significant effect on molten areas.

More in detail, a quasi-parabolic evolution of molten surfaces (S_m = f (VED^2)) is found for bead-on-plate tests (with S_m ranging between 80 to 80,000 μm^2), and L-PBF beads (with S_m between 150 and 65,000 μm^2) with larger error bars in the latter case traducing stronger melt pool fluctuations. Interestingly, below 70 J/mm^3, molten areas are larger for L-PBF beads whereas above 70 J/mm^3 larger areas are obtained when the laser interacts directly with the metal substrate. The differences between bead-on-plate and powder bed molten areas may be explained as follows:

- As calculated and measured respectively in (Boley et al., 2015, 2016), a powder bed has a two to three times higher absorptivity than the flat surface of the same material. A powder bed is also about a hundred times less thermally conductive than the solid substrate of the same material. For L-PBF conditions at low VED and hence for low penetration in the substrate, powder bed properties will strongly govern the molten areas values. Therefore, individual grains tend to reach higher temperatures, resulting in larger melt pools than bead-on-plate fusions (regardless of their distribution below or above the substrate).
- With increasing VED, the penetration into the substrate becomes more and more important and so does the global absorptivity. Powder bed properties have less influence as the upper molten area represent a smaller portion of the final bead area. Thus, for increasing VED and especially for VED between 55 and 80 J/mm^3, the induced molten areas are close in both configurations.
- For very high VED, L-PBF areas are smaller (-20 % on S_m at 113 J/mm^3) than bead-on-plate ones. This could be attributed to the occurrence of more spatters at high VED as shown by (Gunenthiram et al., 2018). Another possible explanation is that the presence of powder, or the motions of the ejected powder are preventing part of

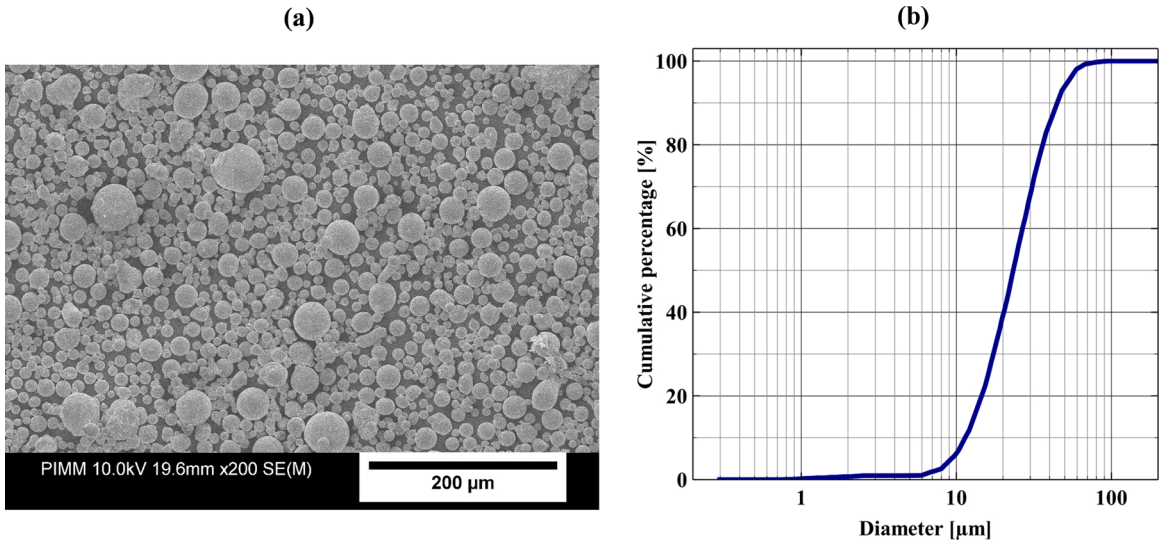

Fig. 4. (a) SEM image of the Inconel 625 powder (x 200) and (b) Particle size distribution.

the laser energy to reach the bulk solid (maybe by scattering or absorbing the incident laser) resulting in lower areas in L-PBF.

3.2. Comparison of on-plate and L-PBF beads dimensions

A deeper focus on powder bed sample dimensions is shown in Fig. 10, where the total depth "e + h", width "w" and height "h" are compared. Near-linear increases of fusion widths and total depths are evidenced for both bead-on-plate and powder bed fusion modes. This linear dependence of molten depths with VED agrees with recent analytical welding models (Fabbro et al., 2018).

Without powder, beads dimensions vary between 50 µm and 300 µm in depth and 180 µm and 420 µm in width. Beads height (above the substrate) are nearly constant around 20 µm. On powder beds, larger (100 µm–290 µm), and deeper (160 µm–350 µm) melt pools are obtained. The bead heights (~ 90 +/-20 µm) are superior to the estimated values (= layer height x powder bed compactness). This is indicative of an additional powder feeding of the single fusion beads from both lateral sides by the denudation phenomena.

As indicated in (Fabbro et al., 2018), the transition from conduction to keyhole welding regime is obtained for aspect ratio r = L/d > 1 (with r = fusion depth / laser diameter). In L-PBF, considering the total fusion depth (height + depth), this ratio is obtained approximately above 40 J/mm^3. This means that for higher VED, the recoil pressure is sufficiently high to deform the liquid surface and initiate a keyhole. Such a VED threshold is significantly higher (~ 60 J/mm^3) on bead-on-plate tests, which indicates a lower vaporisation rate to a faster heat dissipation.

3.3. High-speed melt pool imaging

Melt pool high-speed imaging was carried out using a 60° inclined camera, with 16 kfps rate. A set of pictures extracted from high-speed videos (500 W - 0.3 m/s) are displayed in Fig. 11.

For both gases, the melt pool is clearly distinguishable from the solidified part of the bead. At the front of the melt pool, the white blur identifies the presence of the laser beam heating and deforming the liquid surface through the recoil pressure effect. Such videos confirm that the laser beam rather interacts with molten metal than directly with the powder. The metal also reaches its vaporisation point as a vapour plume is emitted. Various ejections of liquid droplets are observed, with larger ones mostly originating from the melt pool front part. Additionally, grains and clusters of powder also are ejected. Either those particles are incorporated into the melt pool or they fall back elsewhere on the powder bed. They may subsequently form inclusions, cause porosities or impair the surface quality of the final manufactured

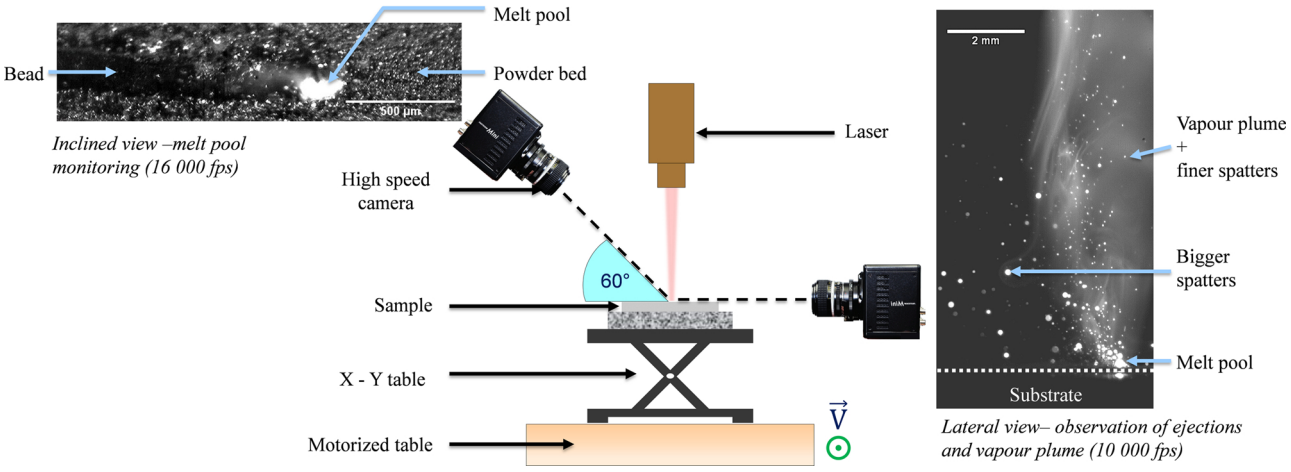

Fig. 5. Schematic of the high-speed-imaging configuration. Left: a 60° inclined camera to observe melt pool and the powder behaviour. Right: a lateral camera allows the observation of the ejections and vaporisation phenomena.

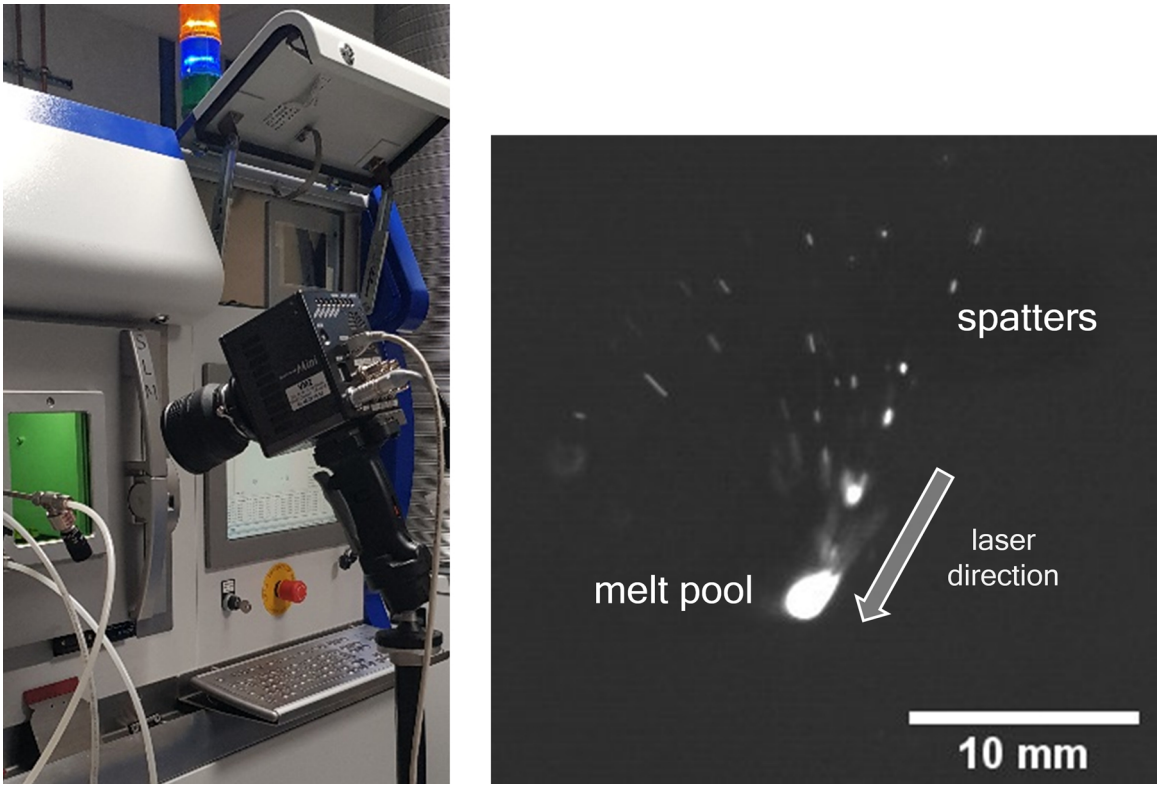

Fig. 6. Photo of the external imaging setup for the SLM 125 machine and image extracted from a low-resolution movie (2000 fps).

part.

The major difference between argon and helium atmospheres involves powder flow around the melt pool. In the videos, it appears that there is more powder motion around the bead under argon. In Fig. 11 pictures, this is identified by more distinct bead contours in helium whereas beads are partly recovered with powder flow under argon. As described by (Matthews et al., 2016) and observed with X-ray imaging in (Guo et al., 2018), a lateral recirculation gas flow is induced by the vertical expansion of vapour plume. That recirculation is one of the origins of the motion of powder located near the interaction zone but not in the direct path of the laser beam. It is considerable near the vaporisation spot (under the laser beam) and decreases further away from the latter. Depending on the flow speed, powder can be dragged from the surrounding bed towards the melt pool creating powder-free areas (denudation areas) around the final bead. (Fig. 12). This reflects an additional indirect fusion mode where powder grains, originally located outside the path of the laser beam, are attracted towards the melt pool and gradually feed it.

3.4. *Analysis of spatters generation*

The side view of the L-PBF process is the most suitable configuration for observing spatters and vapour plume (Fig. 5). Two types of spatters are evidenced during L-PBF single beads: (1) the finer ones (< 40 µm in diameter) are ejected vertically, dragged by the plume ascension; (2) the larger spatters (40–180 µm in diameter) are ejected towards the rear of the melt pool (Fig. 5, right). In bead-on-plate tests, almost no spatters are shown.

Using high-speed imaging, the analysis of spatters number and speed was made under both protective atmospheres, by considering highly emissive (white) particles detected at the focus plane of the camera. The number of spatters was assessed with *ImageJ*, an image

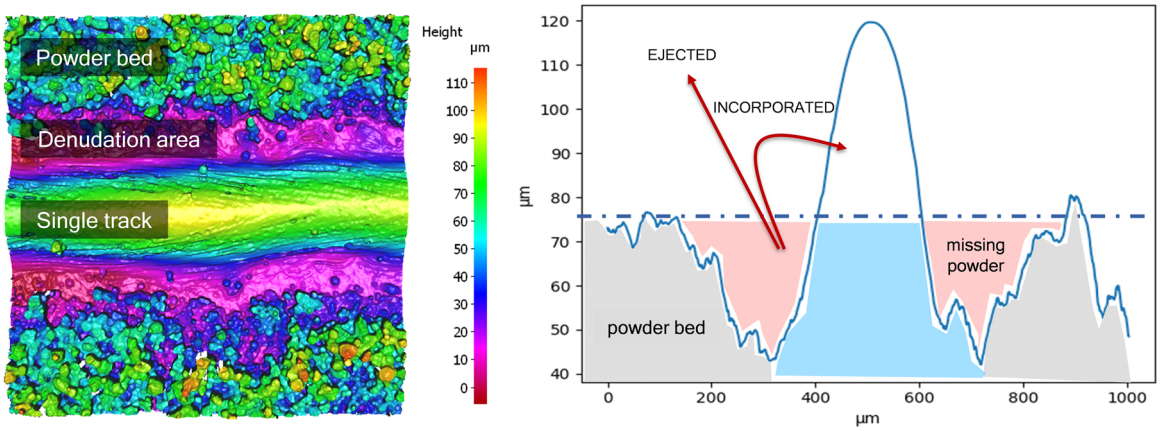

Fig. 7. Optical profilometry map of a single bead of Inconel 625 and its surrounding powder bed. Denudation zones are shown in the powder bed. Profile showing the missing powder areas and the bead morphology.

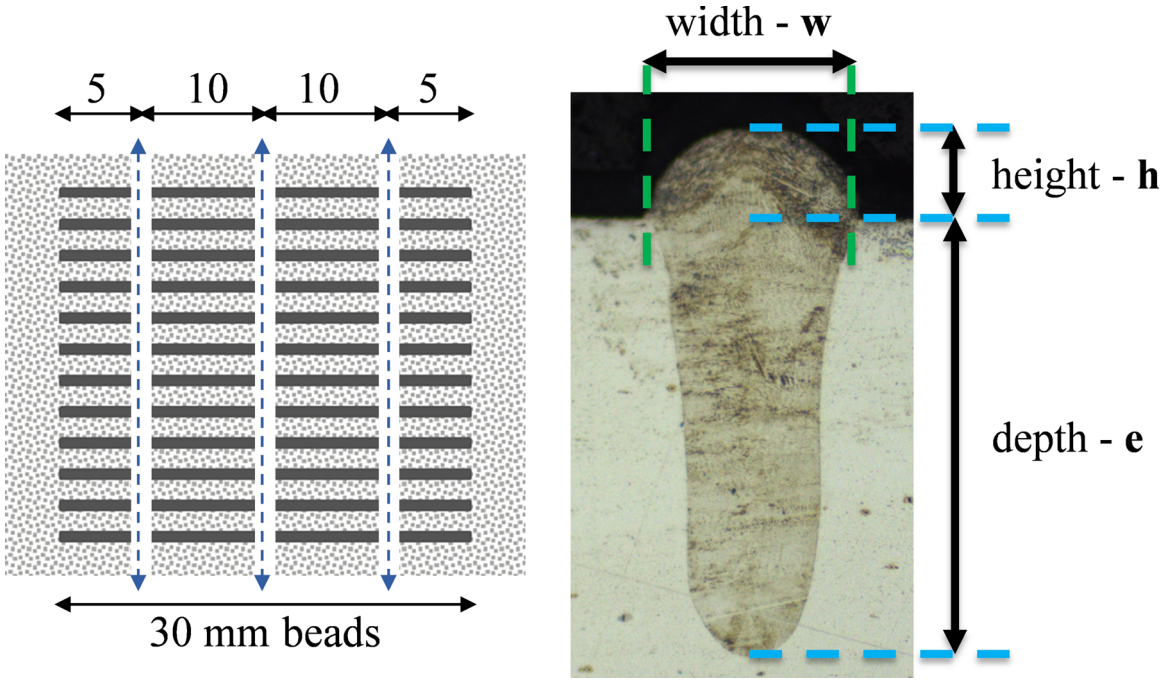

Fig. 8. Schematic description of the morphologic analysis.

processing software. A similar size distribution was found for the two gases, with ejected particles in a range of diameter from 30 to 240 µm, with a mean value around 80 µm. This method was compared with manual counting to confirm its relevance and an average 10 % error margin was found.

Under argon, the number of spatters increases from 700 to 2000 particles between 20–75 J/mm^3 then stabilizes above. With helium, the number of particles reaches a maximum around 700 particles at 50 J/mm^3 and then decreases. Finally, three to four times more ejected spatters are counted in argon than in helium, especially for volume energy density superior to 70 J/mm^3 (Fig. 13). However, use of such a method is to some extent questionable for comparing the influence of argon and helium on spattering because, due to the higher conductivity of helium, ejected particles are expected to cool down faster during their time of flight and be less emissive on the videos. A simple estimation of the heat diffusion volume shows that cooling with helium is 30 times more effective than with argon. On the other hand, the gas around the vapour jet is also hot (around 2000–3000 K) so it remains

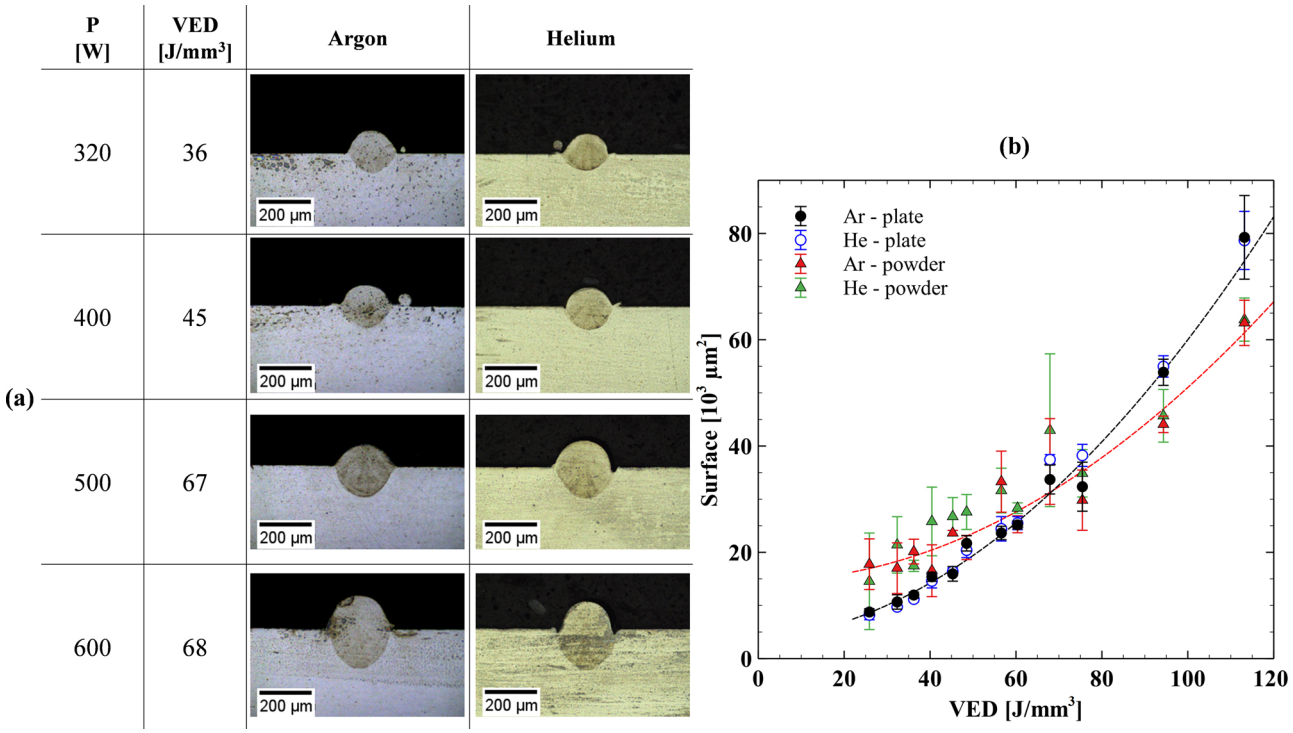

Fig. 9. (a) Macrographs of Inconel 625 powder bed fused beads under Ar and He gases at a speed of 0.5 m/s, (b) Molten surface S_m versus VED for bead on-plate (circles) and powder bed (triangles) fused beads under Ar and He gas. Polynomial regression (deg = 2) are shown as dotted lines (d = 150 µm, top-hat).

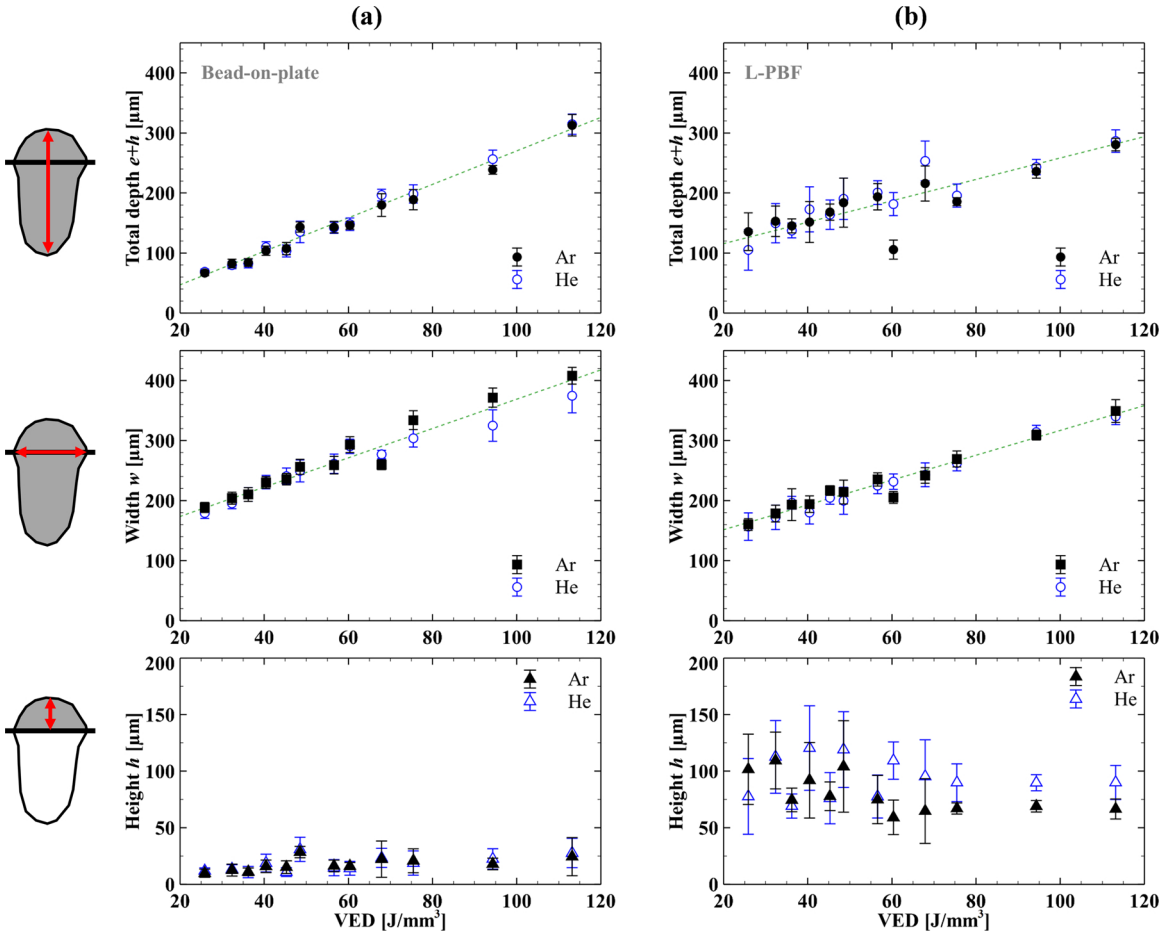

Fig. 10. Evolution of depth (circles), width (squares) and height (triangles) of beads under Ar (full black markers) and He (empty blue markers) gas as function of the VED (d = 150 µm, top-hat) for (a) bead-on-plate and (b) L-PBF tests. (For interpretation of the references to colour in this figure legend, the reader is referred to the web version of this article.)

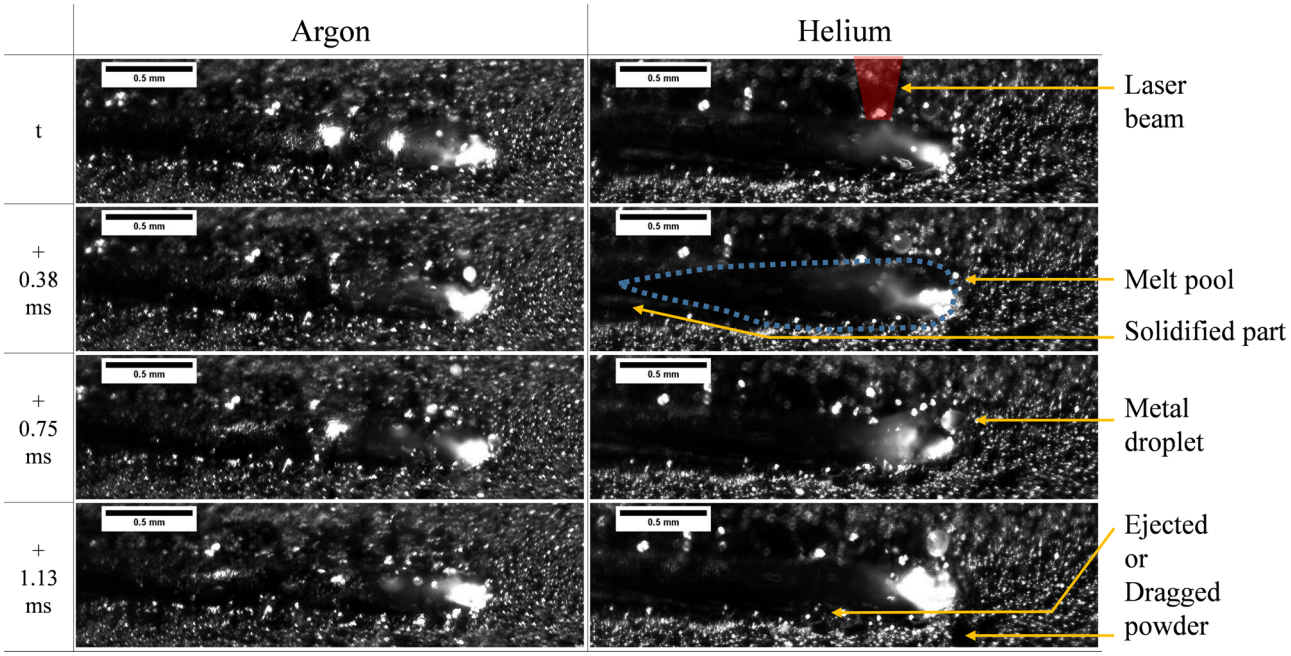

Fig. 11. Set of images extracted from high-resolution videos at 16 000 fps (P_0 = 500 W – V_0 = 0.3 m/s) for Ar and He atmospheres, (0.375 ms between two displayed images).

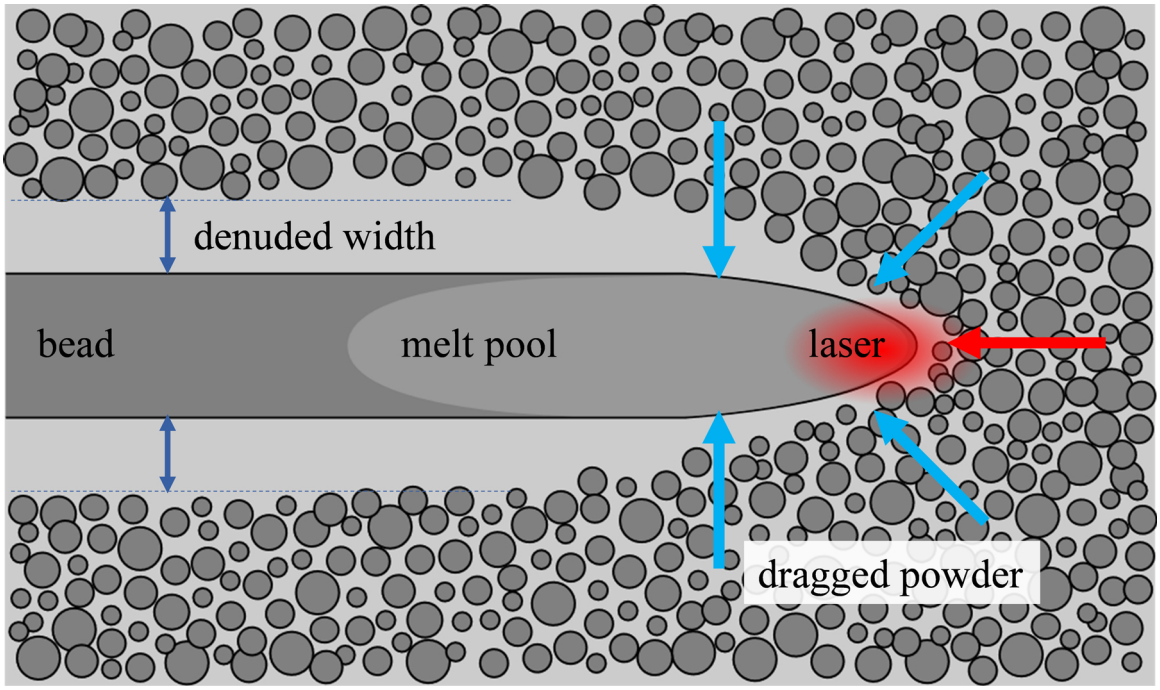

Fig. 12. Schematic description of the powder movements around the melt pool creating denuded areas around the bead.

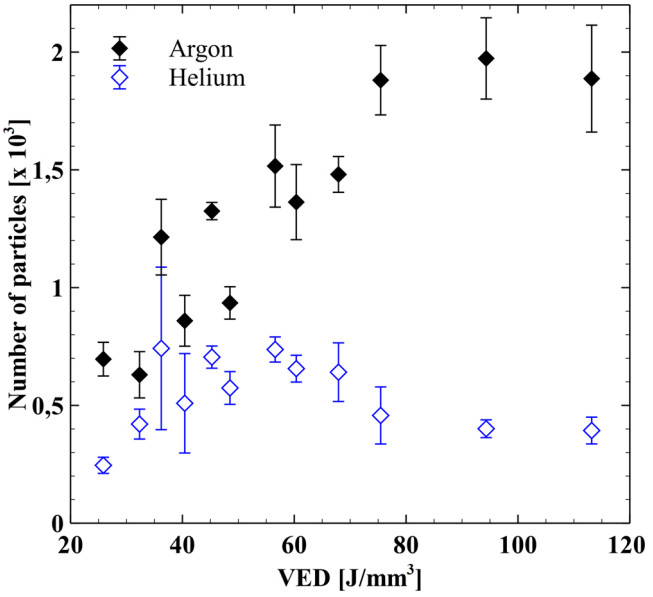

Fig. 13. Number of ejected spatters as a function of the VED under Ar and He atmospheres.

difficult to quantify reasonably these two antagonistic effects without reliable numerical simulations.

3.5. Denudation widths

Areas of missing powder around each bead are clearly visible (Fig. 14). Their width w_{den} was measured using optical profilometry and optical microscopy and the fraction of missing powder was evaluated after processing on *ImageJ* software. It was calculated considering a total surface of area - w_{den} x 1- mm^2 (Fig. 14.c) as the ratio of the empty surface to the total analysed surface.

Denudation widths and efficiency versus VED are presented in Fig. 15. First, denudation widths are greater under argon (330 µm in average) than under helium (144 µm in average), whatever the VED. The denudation efficiency rate is also constant with VED. For a given width, the proportion of missing powder is slightly higher under helium: 38 % against 30 % under argon. This is consistent with observations from the melt pool imaging (paragraph 3.3) where it appeared clearly that, with argon shielding, more powder was dragged from the surroundings of the beads toward the melt pool.

3.6. Analysis of the vapour plume

The vapour plume is mostly composed of evaporating metal elements and hot ambient gas. Depending on its temperature, composition and density, the plume is more or less emissive and visible in high-speed movies. In side view video configuration (Fig. 5, right), and using three VED (26, 68 and 113 J/mm3), one can see clearly that the type of gas affects the shape and aspect of the vapour plume (Fig. 16).

Under argon, a large volume of vapour expands as a cloud whereas under helium it takes the form of a strongly oriented vapour beam. This suggests a faster expansion speed under helium due to its lower density (Mayi et al., 2019). In that case, the vapour is expanding freely and is less confined by the surrounding gas than in argon.

Condensates and spatters generated in argon and helium during L-PBF were collected on a glass slide (cf 2.3.2) to investigate the vapour composition through the SEM-EDS analysis of condensed material. Scans of the glass slides are shown in Fig. 17.

Around the central laser path, ejected particles and deposited matter are clearly evidenced. Under argon, more spatters are collected and the condensed vapours appears darker than under helium. These observations are consistent with the more visible plume under argon gas. The mass of deposited particles and vapour condensates with argon or helium was estimated by weighing the glass slides before and after single bead fusion. The collected mass increases with laser power and is more important under argon shielding (Fig. 18.a). This result consolidates the trend of an amplified spattering under argon. The weighted mass is predominantly the mass of macroscopic spatters as no mass could be detected during on-plate beads (without powder and spatters) even with a 10^{-6} g sensitivity weight scale. Using previously calculated bead surfaces (Fig. 9), it was then possible to estimate the fraction of ejected volume in relation with the total volume of the bead (for a 30 mm long

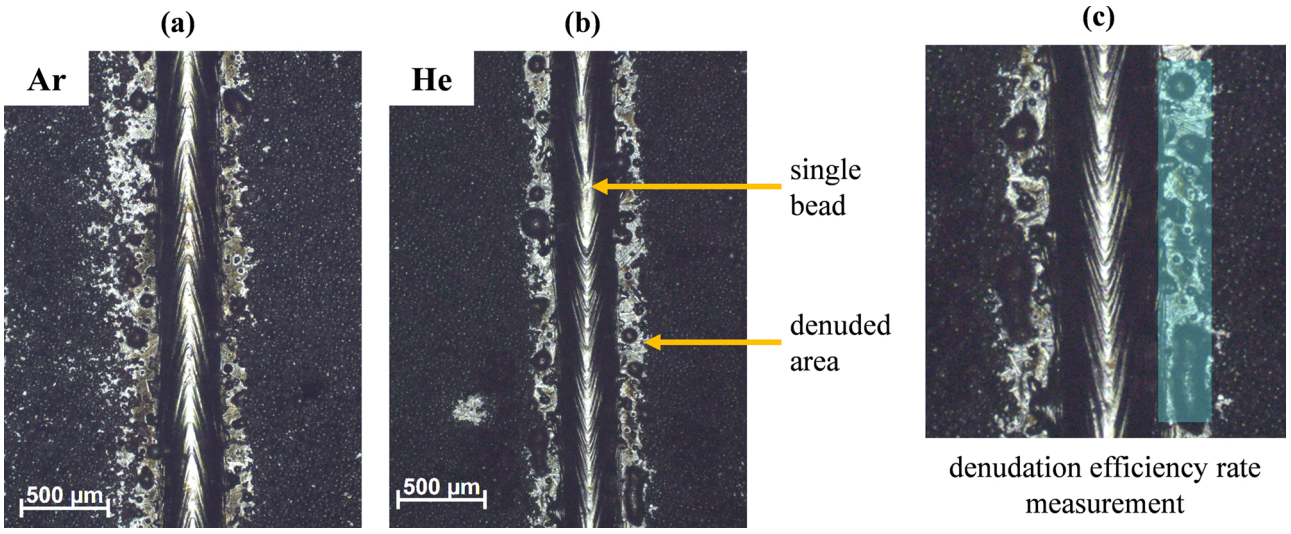

Fig. 14. Influence of gas shielding (a) Ar and (b) He on denudation in the instrumented cell (P_0 = 600 W, V_0 = 0.3 m/s); (c) illustration of the total surface (blue) considered for the efficiency rate measurement. (For interpretation of the references to colour in this figure legend, the reader is referred to the web version of this article.)

bead). This fraction is fluctuating around 6% under argon and around 3% under helium (Fig. 18.b).

At high SEM magnification (Fig. 19), particles constituting the condensed material were found to have diameters in the nanometre range, with near pentagonal shapes. However, particles obtained with argon exhibit a minimum size around 30 nm versus less than 10 nm size with helium. This suggests a shorter time of vapour condensation / agglomeration-coalescence during its expansion in helium due to a faster plume expansion and a higher thermal diffusivity in helium, favouring larger thermal dissipation.

4. Experimental results in SLM 125 HL machine

4.1. Spatters generation and denudation analysis

When observing the process in the industrial L-PBF machine for argon and helium shielding, the first noticeable observation, with low-resolution high-speed videos, is that more spatters are produced under argon atmosphere (Fig. 20). They also appear larger and brighter. The same observation was made on the instrumented setup (paragraph 3.4).

The nature of the protective atmosphere also has a clear impact on the denudation phenomena. After fusion, L-PBF samples were analysed with optical microscopy to evaluate denuded areas, clearly observed all along the bead sides (Fig. 21).

Denuded widths range between 160 µm and 260 µm, being 2–3.5 times larger than the laser beam diameter (Fig. 22), and do not vary with VED. However, contrary to results obtained in the L-PBF small cell (paragraph 3.5), results in the L-PBF machine exhibit a more pronounced denudation in argon. The most significant effect of gas shielding is found in the denudation efficiency, for which the missing powder represents an 8% average surface ratio under argon whereas it goes up to 25 % under helium. This indicates that, under helium, ensuring a good overlapping between adjacent beads might be difficult for classical hatch distances, because of the lack of powder.

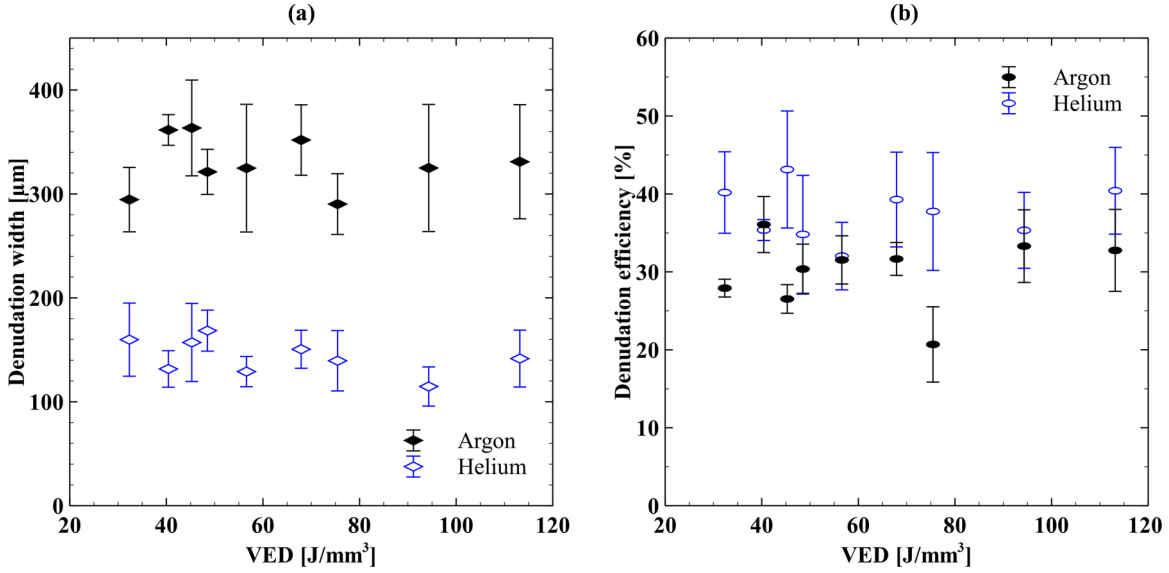

Fig. 15. Denudation width (a) and denudation efficiency (b) as a function of VED for L-PBF beads produced in the instrumented setup (d = 150 µm, top-hat distribution).

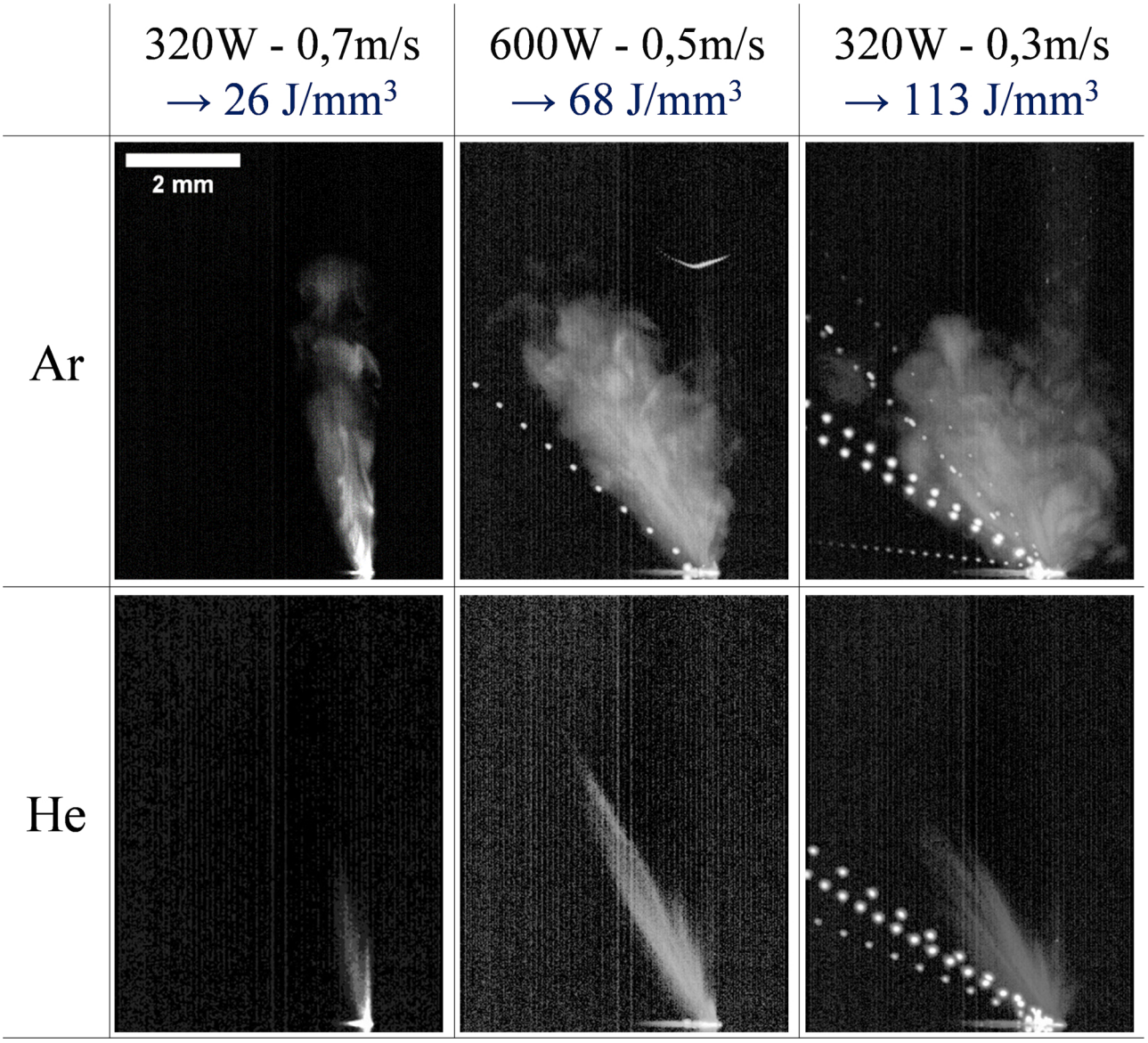

Fig. 16. Overlay of 300 images from video recorded at 10,000 fps (bead-on-plate tests) showing the vapour plume expansion under Ar and He.

4.2. Beads areas and dimensions

The global beads dimensions have also been analysed from macrographs (Fig. 23.a). Just like experiments carried out in the small cell (Fig. 9.a) beads are, at first sight, very similar (global shapes and wetting angles) in both gases.

Detailed dimensions of the beads are presented in Fig. 23.b, The total depths "e + h" are identical in argon and helium atmospheres. Their evolution is linear with the increasing VED: from 130 µm at 50 J/mm^3 to 420 µm at 150 J/mm^3. However, beads manufactured under helium atmosphere are found to be higher (part above the substrate) and narrower in comparison with argon ones. This difference in height might be related to the denudation effects described previously.

Additionally, the total melted area is also equal for the two gases

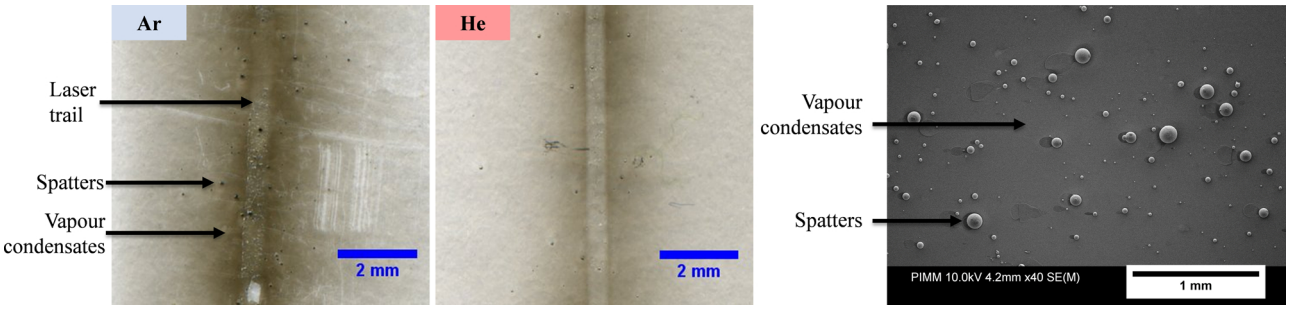

Fig. 17. Images of the glass slides for beads at 400 W and 0.5 m/s under Ar and He (left). Low magnification SEM images of vapour condensates and particles collected on a glass slide (right).

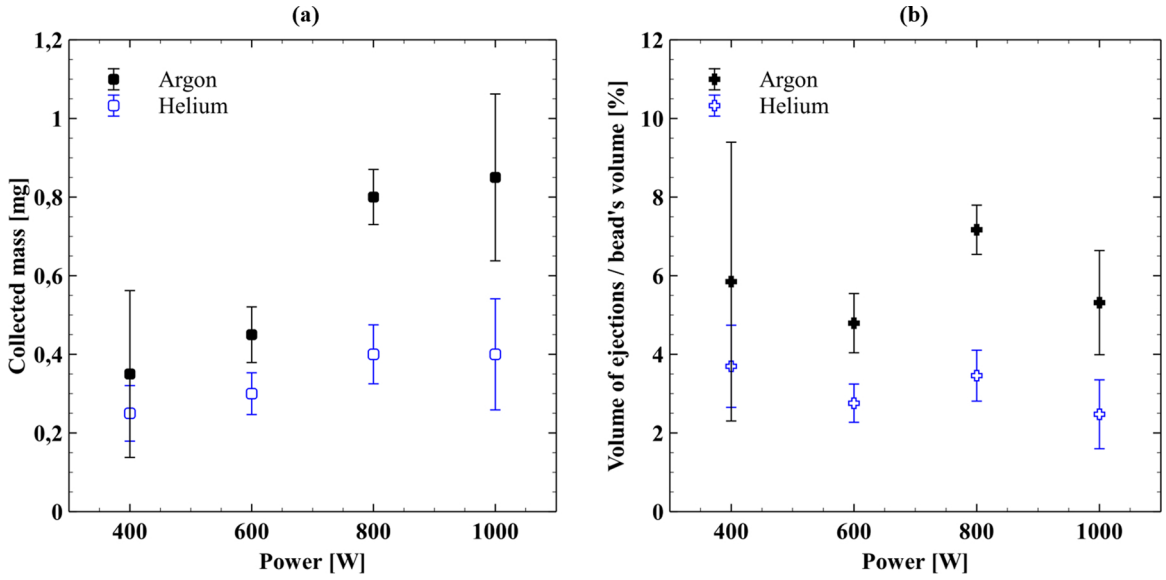

Fig. 18. (a) Mass of ejected particles collected for beads realised at P_0 = 400, 600, 800 and 1000 W at V_0 = 0.5 m/s under Ar and He protections, (b) corresponding volume fractions (related to the total beads' volume).

(Fig. 24.a), which indicates an equivalent energy transfer, a similar absorbed laser energy producing the same volume of melted matter. However, the fraction of bead above the substrate (built volume) is slightly larger in helium than in argon (Fig. 24.b), which indicates that an important fraction of missing powder around the bead has been incorporated in the melt pool (Fig. 7) resulting in a higher bead and a larger upper bead surface under helium shielding. Consequently, in helium, the fraction of laser energy consumed for powder melting is higher than in argon, mainly due to the enhanced melt pool feeding (denudation) by the surrounding powder. Accordingly, less energy is available to melt the substrate.

5. Discussion

5.1. Summary

The influence of shielding atmosphere has been addressed in this paper. Globally, little effects were found on the geometry and molten areas of single beads. This demonstrates a rather similar laser absorption on the melt pools, and through the vapour plumes in spite of higher plume velocities under helium, and a plume composed of smaller nanoparticles.

Two kinds of L-PBF single bead experiments have been made, either on a dedicated cell, with a fixed laser beam, or in an industrial L-PBF machine, with a scan head. The influence of gas shielding on denudation widths was found to be different in the L-PBF cell (low effect of the atmosphere) and in the L-PBF machine (more severe denudation in helium). Moreover, for both experimental configurations, less spatters have been observed with helium shielding. These phenomena are discussed further in Section 4.3.

5.2. Argon versus helium

On the one hand, a similar energy coupling (same molten area S_m) has been found between argon and helium, indicating that the laser absorption (in the liquid, through the vapour plume) is kept constant, and that the boundary conditions (ten times higher conductivity of helium) did not play a dominant role.

On the other hand, in the L-PBF machine, a stronger denudation was obtained in helium, resulting in a larger energy consumption in the powder bed, compared with argon shielding (Fig. 25). This is materialised by larger upper parts for single beads produced under helium.

This phenomenon was also pointed out experimentally by (Bidare, 2018) and suspected by (Mayi et al., 2019) using numerical simulation. During the keyhole formation and the vaporisation of the metal, a radial flow (of protective gas) directed toward the melt pool is induced

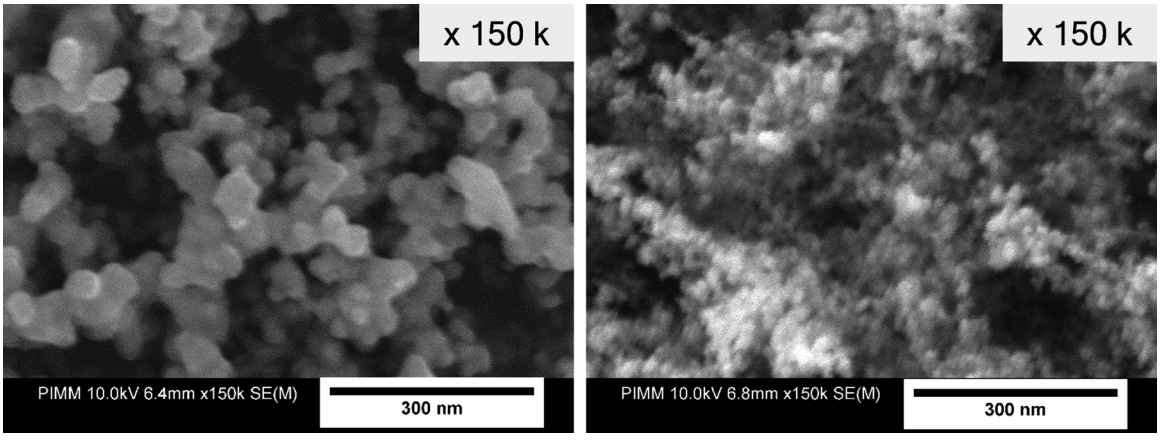

Fig. 19. Observation at x150k magnification of the condensed material (left) for Ar and (right) for He atmospheres.

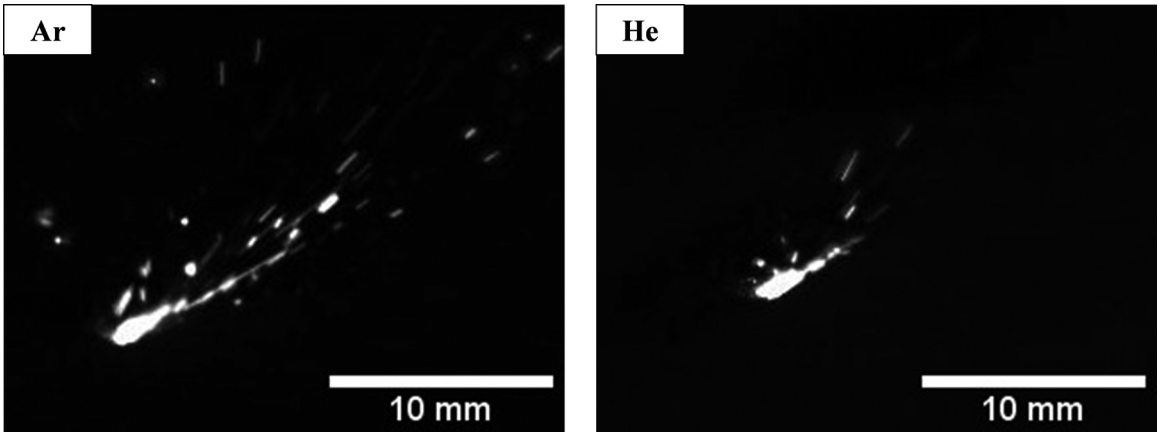

Fig. 20. Images extracted from low-resolution imaging of single beads produced in the SLM 125 machine at P_0 = 300 W and V_0 = 0.75 m/s under (left) Ar and (right) He atmospheres.

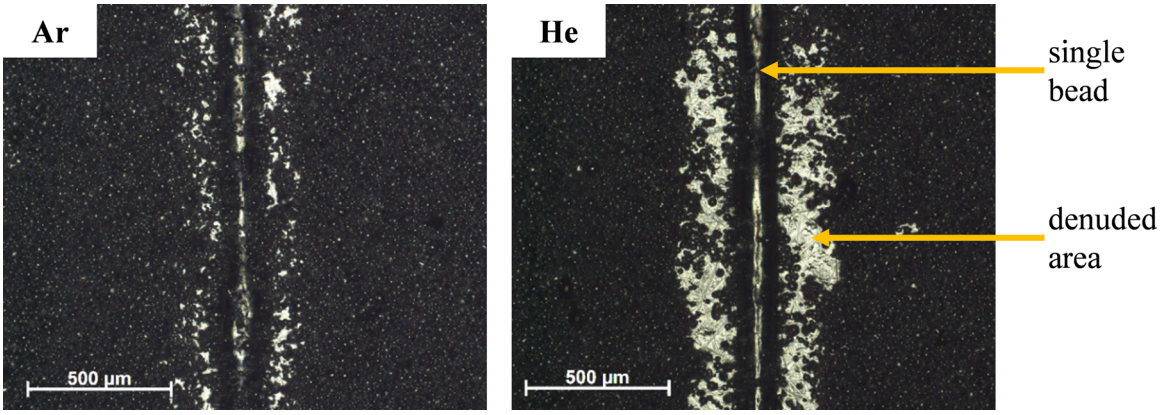

Fig. 21. Influence of gas shielding: (left) Ar and (right) He on denudation (at P_0 = 200 W, V_0 = 0.75 m/s) for beads produced in the SLM 125 machine (d = 73 µm, Gaussian).

(Matthews et al., 2016) which is the dragging force for denudation. Because the associated speed flow was found to be approximately two times faster under helium because of its lower density (Mayi et al., 2019), the resulting dragging force $F_t \propto 1/2\ \rho S U^2$ (for a particle of projected surface S in a gas of density ρ and velocity U) is therefore able to transport more powder towards the melt pool in helium. That enhanced powder feeding under helium is responsible for the difference in morphology: L-PBF beads are comparatively larger in their upper part (Fig. 24).

Surprisingly, more spatters have been systematically observed in

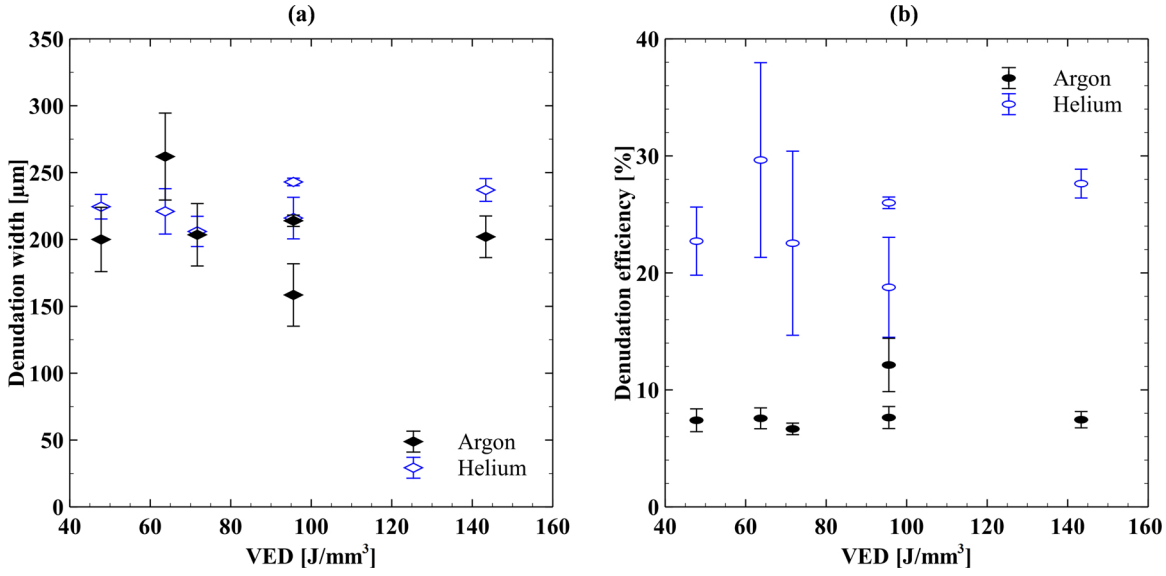

Fig. 22. Denudation width (a) and denudation efficiency (b) as functions of VED for beads produced in the machine.

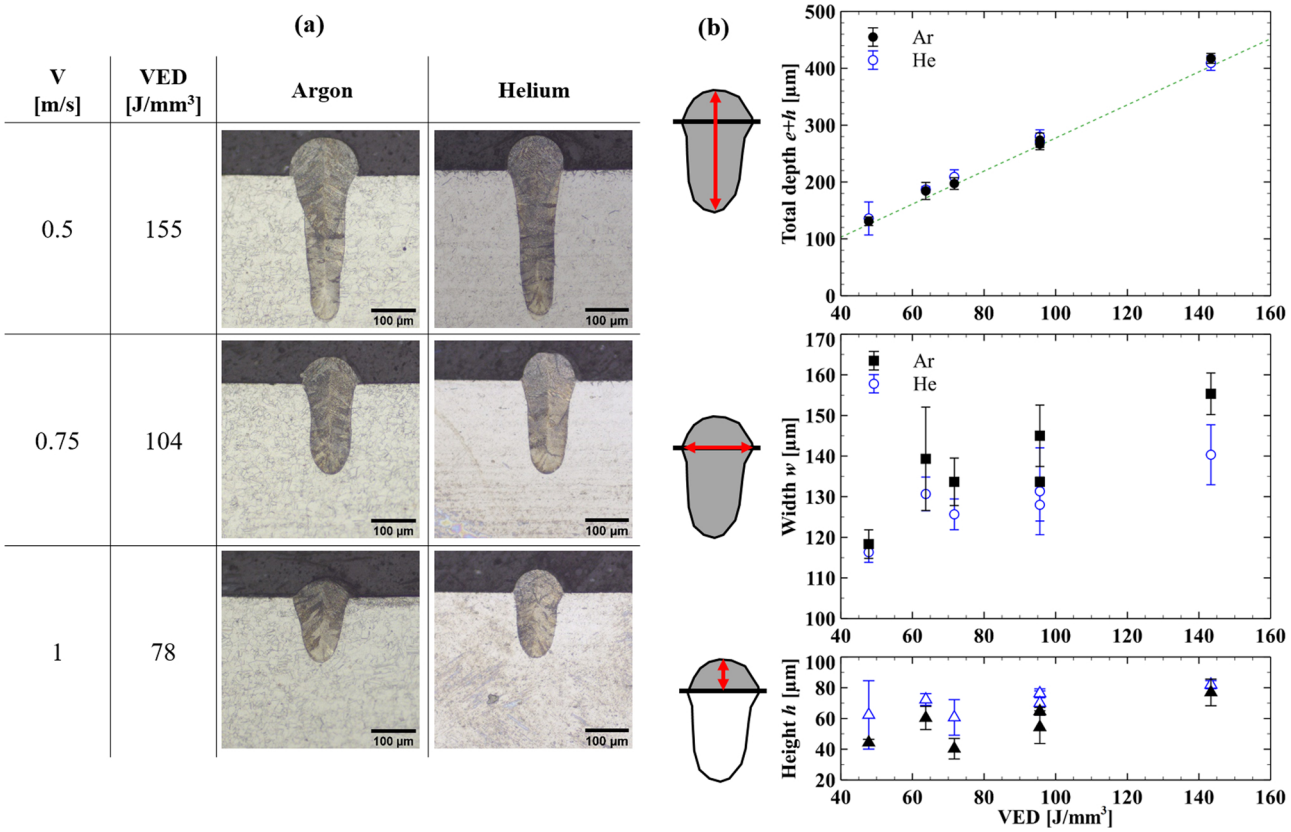

Fig. 23. (a) Macrographs of Inconel 625 powder-bed beads under Ar and He in the SLM 125 (P_0 = 300 W, D = 73 µm), (b) Evolutions of depth (circles), height (triangles) and width (squares) of beads under Ar (full black markers) and He (empty blue markers) gas as function of the VED (d = 73 µm, Gaussian) in machine. (For interpretation of the references to colour in this figure legend, the reader is referred to the web version of this article.)

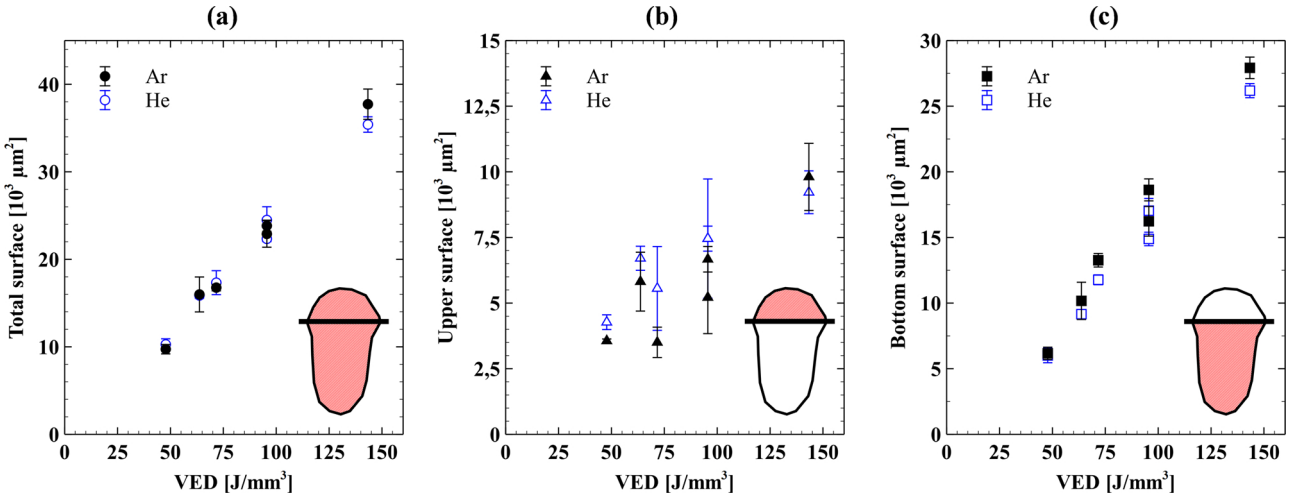

Fig. 24. Evolution of (a) total surface (circles), (b) upper surface (triangles) and (c) bottom surface (squares) of beads under Ar (full black markers) and He (empty blue markers) gas as a function of VED (d = 73 µm, Gaussian) in machine. (For interpretation of the references to colour in this figure legend, the reader is referred to the web version of this article.)

argon (around 6 % of the global melt volume) than in helium (3 %) (Fig. 18, Fig. 20), whatever the used set up, and in spite of a reduced denudation limiting the powder feeding. This phenomenon is not fully understood yet, but preliminary analysis of the surface finish of L-PBF cubic samples carried out under Helium have revealed better average roughness, which tends to confirm the lower spatter amount. Oncoming analyses (density, microstructures) will complete the current work to provide a more global understanding of gaseous effects, including both local approach (near the melt-pool, during the interaction), and post-mortem properties.

Finally, the possible use of helium instead of argon still has to be investigated at the scale of a full 3D part to draw global conclusions. From the current study, it appears that the only apparent benefit of using helium is that it generates significantly less spatters. This might result in improved surface finish and reduced inclusion ratio in the built volumes. It is also worth questioning if beads with high upper parts like those produced under helium, combined with larger denudation areas will overlap successfully to ensure an optimal density to the built part.

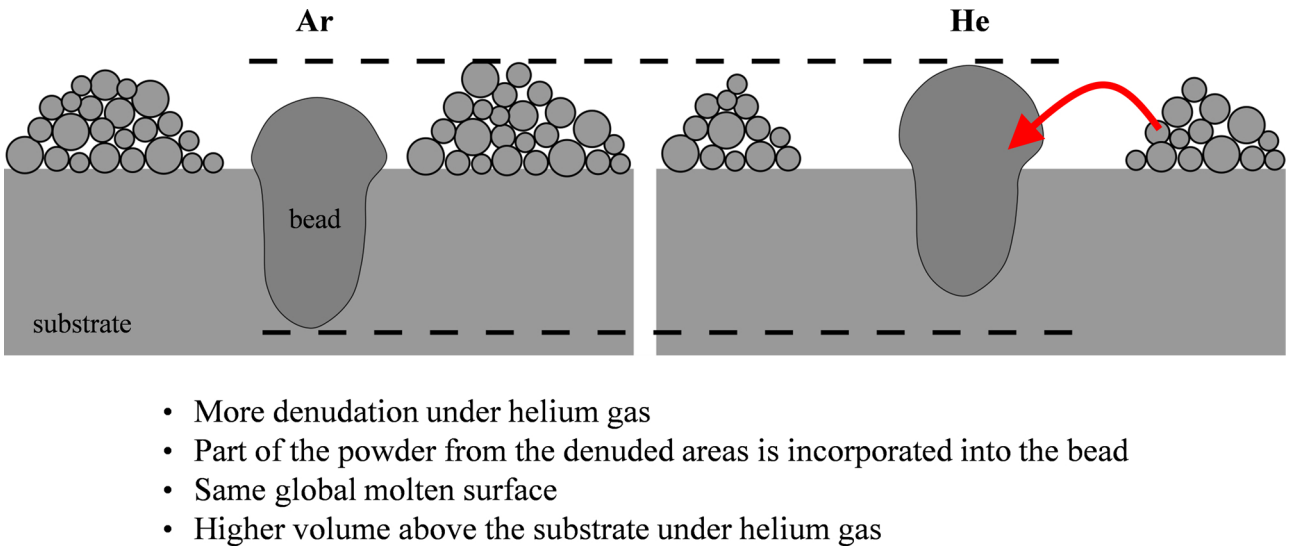

Fig. 25. Beads morphology due to difference in denudation phenomenon under Ar and He atmospheres. More powder is dragged under He resulting in bead with higher upper parts.

Oncoming trials will investigate this aspect, including an optimization of hatch distance.

As the melt pools characteristics are mainly governed by the metal properties at liquid state including the surface tension at the liquid - vapour interface, the previous results of beads morphology could be extended to other Ni-based alloys of close chemical composition. Concerning the aerodynamics of vapour plume, denudation and spattering, it should be very similar too for other Ni-based superalloys carried out with the same powder and powder bed characteristics.

Lastly, because of its low density, helium also has a lower confining ability. Generated nanoparticles (Fig. 19) are reaching easily the top part of the working chamber and generate a strong contamination of the building chamber and the laser optics (Charpentier et al., 2018). This might be problematic in the case of several hours of production. Practically, due to its low density, inerting the working chamber is also taking longer time than under argon. Last, but not least, helium is substantially more expensive than argon. For all these reasons, pure helium will certainly not replace argon in L-PBF in the coming years.

5.3. Comparison of the two setups

Using a static laser beam is potentially attractive because it facilitates high-speed imaging of molten pools during L-PBF, compared to a classical (with scan head) industrial machine. However, differences have been observed, especially concerning denudation effects: no significant difference was shown between argon and helium in the small moving L-PBF set-up, contrary to the L-PBF machine. As a reminder, the main differences between the used set-ups (small cell and industrial machine) are: (1) the laser distribution (top hat versus Gaussian), (2) the laser/powder bed relative motion and (3) the working chamber volume (around 2 L for the cell and 50 L for the machine)

The difference observed between the two setups might be linked to the energy distribution of the laser beam (Gaussian versus top-hat). (Metel et al., 2018) studied the influence of the laser power distribution for L-PBF single beads of a CoCrMo alloy including Gaussian, top hat and donut distributions. Even if they observed globally similar denuded widths with Gaussian or top hat laser distributions, the (denuded width/ laser diameter) ratio was two times larger for the Gaussian beam diameter. This result is partly confirmed here, where (denuded width/ laser diameter) ratios are around 1–2 for the d = 150 µm top-hat (Fig. 15) and 3 for the d = 73 µm Gaussian (Fig. 22). This could explain why lateral areas were comparatively larger and more denuded in the current work for a d = 73 µm Gaussian spot than for a d = 150 µm top-hat laser. This assumption should be checked in future work by considering a Gaussian irradiation – fixed laser beam in the small experimental cell.

Another explanation for the differences between the two setups might be the difference in aerodynamics in the two working chambers because : (1) with the instrumented cell, the whole setup is moving at a speed up to 1 m/s whereas in the machine, the chamber is static, (2) the machine chamber has a 25 times greater volume than the cell. Thus, the gas flow and the related consequences (ejections, denudation) might appear differently.

6. Conclusions

The current results are providing a new insight about the influence of gas in the L-PBF process as it was rarely studied in previous works. Switching the gaseous atmosphere from argon to helium in the manufacturing process was shown to influence the main phenomena surrounding the melt pool like material vaporisation, spattering or powder denudation, but not the laser absorption and resulting energy coupling.

With helium shielding, a reduction of spatters, an increase of the vapour plume speed and a modification of the vapour composition (smaller nanoparticles due to higher thermal conductivity) were observed. The lower density of helium also promoted denudation phenomena, because of higher speed induced gas flow, generating larger built volumes (but no larger fused volumes) than in argon.

In addition, the use of an experimental and instrumented setup allowed using more diagnoses than inside an industrial L-PBF machine. However, experiments carried out in a small moving cell with a static laser beam in comparison has revealed some differences (denudation phenomenon) with L-PBF conditions tests. This is also raising the question of the extent to which L-PBF devices can be simplified while remaining representatives of the reality of the process. In spite of differences of denudation, attributed to the different laser beam distributions, such a setup was accurate for analysing physical phenomena involved in L-PBF and performing high-speed imaging. Oncoming work will be extended to the analysis of 3D parts built using helium and argon. Lastly, the presented study allowed specifying a method with criteria to qualify gases for the L-PBF process. Indeed, in single bead configuration such a methodic experimental approach could be easily extended to the study of other atmospheres, other materials and to a wider range of process parameters too.

Declaration of Competing Interest

The authors declare that they have no known competing financial interests or personal relationships that could have appeared to influence the work reported in this paper.

Appendix A. Supplementary data

Supplementary material related to this article can be found, in the online version, at doi:https://doi.org/10.1016/j.jmatprotec.2020.116851.

References

Ahn, J., He, E., Chen, L., Dear, J., Davies, C., 2017. The effect of Ar and He shielding gas on fibre laser weld shape and microstructure in AA 2024-T3. J. Manuf. Process. 29, 62–73. https://doi.org/10.1016/j.jmapro.2017.07.011.

Air Liquide, 2020. Encyclopédie Des Gaz Encycl. Gaz. URL. https://encyclopedia.airliquide.com/fr.

Andreau, O., Pessard, E., Koutiri, I., Penot, J.-D., Dupuy, C., Saintier, N., Peyre, P., 2019. A competition between the contour and hatching zones on the high cycle fatigue behaviour of a 316L stainless steel: analyzed using X-ray computed tomography. Mater. Sci. Eng. A 757, 146–159. https://doi.org/10.1016/j.msea.2019.04.101.

Anwar, A.B., Pham, Q.-C., 2017. Selective laser melting of AlSi10Mg: effects of scan direction, part placement and inert gas flow velocity on tensile strength. J. Mater. Process. Technol. 240, 388–396. https://doi.org/10.1016/j.jmatprotec.2016.10.015.

Bidare, P., Maier, R.R.J., Beck, R.J., Shephard, J.D., Moore, A.J., 2017. An open-architecture metal powder bed fusion system for in-situ process measurements. Addit. Manuf. 16, 177–185. https://doi.org/10.1016/j.addma.2017.06.007.

Bidare, P., Bitharas, I., Ward, R.M., Attallah, M.M., Moore, A.J., 2018. Laser powder bed fusion in high-pressure atmospheres. Int. J. Adv. Manuf. Technol. 99, 543–555. https://doi.org/10.1007/s00170-018-2495-7.

Boley, C.D., Khairallah, S.A., Rubenchik, A.M., 2015. Calculation of laser absorption by metal powders in additive manufacturing. Appl. Opt. 54, 2477. https://doi.org/10.1364/AO.54.002477.

Boley, C.D., Mitchell, S.C., Rubenchik, A.M., Wu, S.S.Q., 2016. Metal powder absorptivity: modeling and experiment. Appl. Opt. 55, 6496. https://doi.org/10.1364/AO.55.006496.

Bosio, F., Aversa, A., Lorusso, M., Marola, S., Gianoglio, D., Battezzati, L., Fino, P., Manfredi, D., Lombardi, M., 2019. A time-saving and cost-effective method to process alloys by Laser Powder Bed Fusion. Mater. Des. 181, 107949. https://doi.org/10.1016/j.matdes.2019.107949.

Charpentier, C., Effinger, M., Lefebvre, P., Briand, F., Edy, F., Abed, S., Peyre, P., 2018. Effect of the Gas Atmosphere During the Laser Beam Melting Process. Presented at the Rapid. Tech Fachkongress, Erfurt, Germany. .

Dai, D., Gu, D., 2015. Effect of metal vaporization behavior on keyhole-mode surface morphology of selective laser melted composites using different protective atmospheres. Appl. Surf. Sci. 355, 310–319. https://doi.org/10.1016/j.apsusc.2015.07.044.

Fabbro, R., Dal, M., Peyre, P., Coste, F., Schneider, M., Gunenthiram, V., 2018. Analysis and possible estimation of keyhole depths evolution, using laser operating parameters and material properties. J. Laser Appl. 30, 032410. https://doi.org/10.2351/1.5040624.

Glowacki, M.H., 1995. The effects of the use of different shielding gas mixtures in laser welding of metals. J. Phys. Appl. Phys. 28, 2051–2059. https://doi.org/10.1088/0022-3727/28/10/009.

Greses, J., Hilton, P.A., Barlow, C.Y., Steen, W.M., 2004. Plume attenuation under high power Nd:yttritium–aluminum–garnet laser welding. J. Laser Appl. 16, 9–15. https://doi.org/10.2351/1.1642636.

Gunenthiram, V., Peyre, P., Schneider, M., Dal, M., Coste, F., Koutiri, I., Fabbro, R., 2018. Experimental analysis of spatter generation and melt-pool behavior during the powder bed laser beam melting process. J. Mater. Process. Technol. 251, 376–386. https://doi.org/10.1016/j.jmatprotec.2017.08.012.

Guo, Q., Zhao, C., Escano, L.I., Young, Z., Xiong, L., Fezzaa, K., Everhart, W., Brown, B., Sun, T., Chen, L., 2018. Transient dynamics of powder spattering in laser powder bed fusion additive manufacturing process revealed by in-situ high-speed high-energy x-ray imaging. Acta Mater. 151, 169–180. https://doi.org/10.1016/j.actamat.2018.03.036.

Hoffman, J., Szymanski, Z., 2004. Time-dependent spectroscopy of plasma plume under laser welding conditions. J. Phys. Appl. Phys. 37, 1792–1799. https://doi.org/10.1088/0022-3727/37/13/010.

Katayama, S., 2010. Understanding and improving process control in pulsed and continuous wave laser welding. Advances in Laser Materials Processing. Elsevier, pp. 181–210. https://doi.org/10.1533/9781845699819.3.181.

Kuo, T.-Y., Lin, Y.-D., 2007. Effects of different shielding gases and power waveforms on penetration characteristics and porosity formation in laser welding of inconel 690 alloy. Mater. Trans. 48, 219–226. https://doi.org/10.2320/matertrans.48.219.

Matsunawa, A., Kim, J.-D., 2006. Basic understanding on beam - plasma interaction in laser welding, in: pacific International Conference on applications of lasers and optics. Presented at the PICALO 2006. In: 2nd Pacific International Conference on Laser Materials Processing, Micro, Nano and Ultrafast Fabrication. Laser Institute of America, Melbourne, Australia. pp. 128–133. https://doi.org/10.2351/1.5056913.

Matthews, M.J., Guss, G., Khairallah, S.A., Rubenchik, A.M., Depond, P.J., King, W.E., 2016. Denudation of metal powder layers in laser powder bed fusion processes. Acta Mater. 114, 33–42. https://doi.org/10.1016/j.actamat.2016.05.017.

Mayi, Y.A., Dal, M., Peyre, P., Bellet, M., Metton, C., Moriconi, C., Fabbro, R., 2019. Laser-induced plume investigated by finite element modelling and scaling of particle entrainment in Laser Powder Bed Fusion (LPBF). J. Phys. Appl. Phys. https://doi.org/10.1088/1361-6463/ab5900.

Metel, A., Stebulyanin, M., Fedorov, S., Okunkova, A., 2018. Power density distribution for laser additive manufacturing (SLM): potential, fundamentals and advanced applications. Technologies 7, 5. https://doi.org/10.3390/technologies7010005.

Shcheglov, P.Y., Gumenyuk, A.V., Gornushkin, I.B., Rethmeier, M., Petrovskiy, V.N., 2013. Vapor–plasma plume investigation during high-power fiber laser welding. Laser Phys. 23, 016001. https://doi.org/10.1088/1054-660X/23/1/016001.

Wang, X.J., Zhang, L.C., Fang, M.H., Sercombe, T.B., 2014. The effect of atmosphere on the structure and properties of a selective laser melted Al–12Si alloy. Mater. Sci. Eng. A 597, 370–375. https://doi.org/10.1016/j.msea.2014.01.012.